Chapter One

Introduction

Chapter Two

Theoretical Considerations

Chapter Three

Results and Discussion

Chapter Four

Conclusions and Recommendations for Future Works

References

Abstract

A theoretical investigation is carried out by using an analytical expression for paraxial trajectory of an electron in a magnetic lens to estimate the optimum properties of the magnetic lens.

The aberration coefficients of the magnetic lens are studied, such as the spherical, chromatic, radial distortion and spiral distortion aberration coefficients. The Glaser's bell-shaped model is adopted to represent the axial field distribution of magnetic lens. The initial momentum of the electrons is taken into account, where the calculations are made for two cases: when the electrons have zero and non-zero initial momentum values .

The optimization role is achieved by changes some of the effective parameters at the range of the half-width at half maximum (a = 2.01, 2.02, 2.03 and 2.04 mm), the maximum magnetic flux density (B_m = 0.001, 0.002, 0.003 and 0.004 Tesla$)$ and the electron emission angle (θ = 0.2, 0.4, 0.5 and 0.6 rad).

In the present results the optimum values for both cases of the initial momentum is found at the half-width at half maximum equal to 2.04 mm, and the values of the spherical, chromatic and spiral distortion aberration coefficients decreased as the half-width at half maximum (a) increased, while the minimum values of the spherical and radial distortion aberration coefficients are found at B_m = 0.004 Tesla in the first case.

However the best angle is found at θ = 0.2 rad which is directly proportional which chromatic and spiral distortion aberration coefficients.

On the other hand the calculations appeared that the negative values for both spherical and radial distortion aberration coefficients are estimated and these coefficients can be used as corrector in the optical systems.

Chapter Three

Results and Discussion

3-1 Introduction

In the present work the analytical method is used to study the optical properties of the magnetic lens which give rise to the minimum aberration coefficients.

The calculations are achieved by writing a computer program using MATHCAD 14. The calculations are divided into two parts: the first, when the initial momentum of electrons is equal to zero, i.e. the electrons start from the object displaced outside the magnetic field. The second, when the initial momentum of electrons doesn't equal to zero.

The optimization is made by changing some parameters as the maximum magnetic flux density and the half-width at half maximum of the magnetic lenses. Also the effect of change the electron emission angle is taken into account in the study of the optical properties when the initial momentum doesn't equal to zero.

3-2 Magnetic Flux Density Distribution

The axial flux density distribution of lens B(z) is computed by using Eq. (2-1) for many values of the maximum magnetic flux density (B_m = 0.001, 0.002, 0.003 and 0.006 Tesla) and the results are shown in figure (3-1).
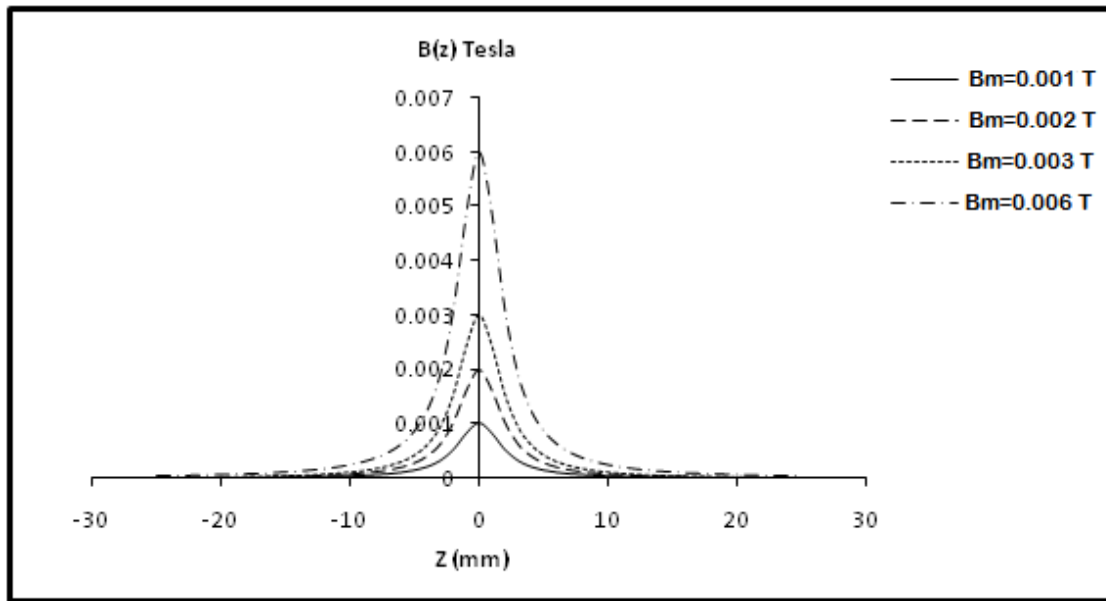
Figure (3-1): Axial flux density distribution of the magnetic lens for
B_m= 0.001, 0.002, 0.003 and 0.006 Tesla.

3-3 Zero Initial Momentum

Different values of the half-width at half maximum (*a*) such as *a* = 1, 1.5, 2, 2.5 and 3 mm are tested and the calculations show that the value of the half-width at half maximum at *a* = 2 mm gives the best results for all aberration coefficients acceptable. Also, it was found that the calculation is very sensitivity to the slightly changing in values of the half-width at half maximum. Therefore, different values of the half-width at half maximum around these values (*a* = 2.01, 2.02, 2.03 and 2.04 mm) are taken into account to find the best results.

3-3-1 The effects of changing the half-width at half maximum

The aberration coefficients are computed for different values of the half-width at half maximum (*a* = 2.01, 2.02, 2.03 and 2.04 mm) at constant maximum magnetic flux density (B_m = 0.001 Tesla) and the results are shown as following:

3-3-1-1 electron beam trajectory

The analytical solution was found for r_b/r_o for equation (2-9) with the Glaser field, electron trajectories (basic trajectories) start normal to the specimen with different values of the half-width at half maximum. The electron beam trajectory along the magnetic field has been computed using Eq. (2-14), and the effects of changing the half-width at half maximum has been investigated at constant values of the maximum magnetic flux density (B_m= 0.001 Tesla) and excitation parameter ($\frac{NI}{\sqrt{V_r}}$)=11.068 (Amp.turn/ (Volt)$^{0.5}$), and the results are shown in figure (3-2).
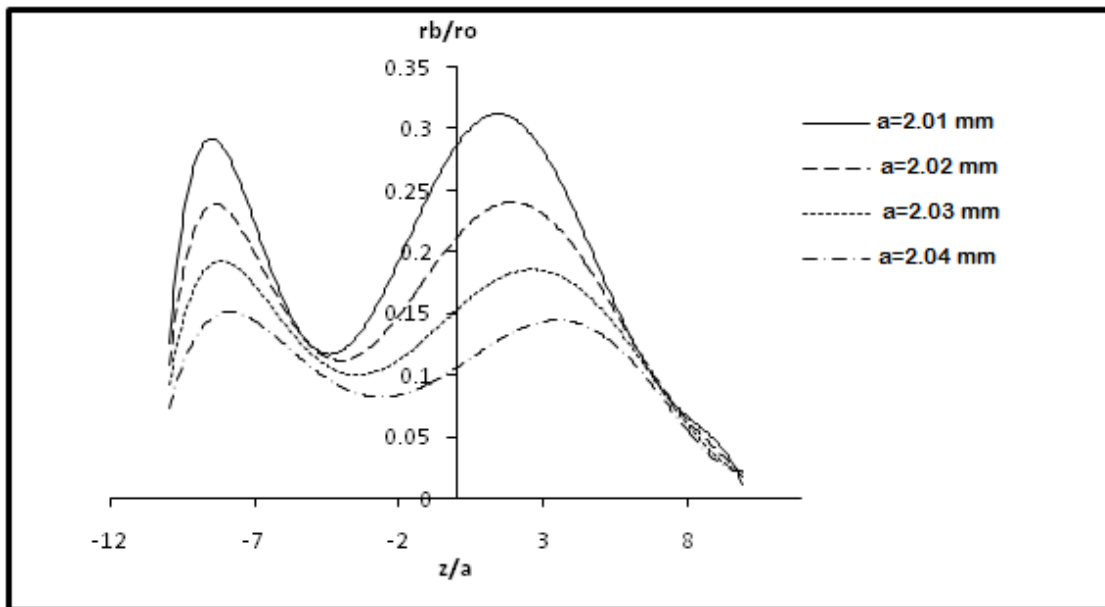

Figure (3-2): Electron beam trajectory for the magnetic lens at excitation
parameter ($\frac{NI}{\sqrt{V_r}}$) =11.068 and B_m= 0.001 Tesla for different values
of the half-width at half maximum (*a*).

The computations appear that when the values of the half width at half maximum (*a)* increase from 2.01 to 2.04 mm the electron beam trajectory becomes smoother, i.e. the fluctuation between the upper and lower values of the displacement from the optical axis is reduced.

The variation in the upper and lower values of r_b/r_o of the trajectory for whole range of the relative optical path z/a is small when the values of the half-width at half maximum (a) are high.

In general the results of the present work illustrated in figure (3-2) have the same behavior as the results of in the work of Melnikov and Potapkin [2].

3-3-1-2 spherical aberration coefficients

The relative spherical aberration coefficients are computed by using Eq. (2-20) and the effects of variation of the half-width at half maximum (a) are studied, as shown in figure (3-3).
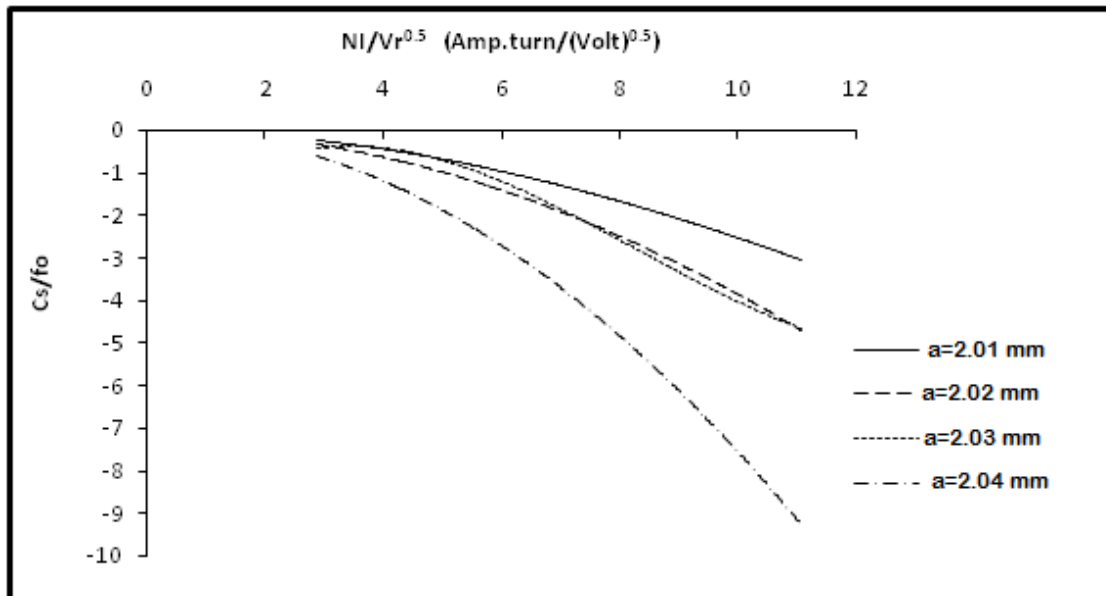

Figure (3-3): Relative spherical aberration coefficients as a function of
the excitation parameter $\left(\dfrac{NI}{\sqrt{V_r}}\right)$ for different values of the half-width
at half maximum.

From this figure one can observed that at the low values of excitation parameter $\left(\dfrac{NI}{\sqrt{V_r}}\right)$, the values of the relative spherical aberration coefficients are closed to each other for different values of the half-width at half maximum, and the relative

spherical aberration coefficients values is diverge at the range of high excitation

parameter $\left(\frac{NI}{\sqrt{V_r}}\right)$.

Also in figure (3-3), the values of the relative spherical aberration coefficients C_s/fo are decreased when the half-width at half maximum (*a*) increases and at the half-width at half maximum (*a* = 2.04 mm) one can find the lowest values. This behavior is shown clearly in figure (3-4), where the relative spherical aberration coefficients are plotted as a function of the half-width at half maximum for constant value of the excitation parameter $\left(\frac{NI}{\sqrt{V_r}}\right)$ = 11.068 (Amp.turn/(Volt)$^{0.5}$).

The results show that the values of the spherical aberration coefficients are negative and this results can be used to design the magnetic lens which can be achieved the role of the corrector in the electron optical system, where the researches in the last 10 years interest by the benefits of the negative spherical aberration coefficients in the design of high resolution electron microscopy [see in 44, 45, 46, 25, 1, 43, 27, 28, 42, 29 and 31].
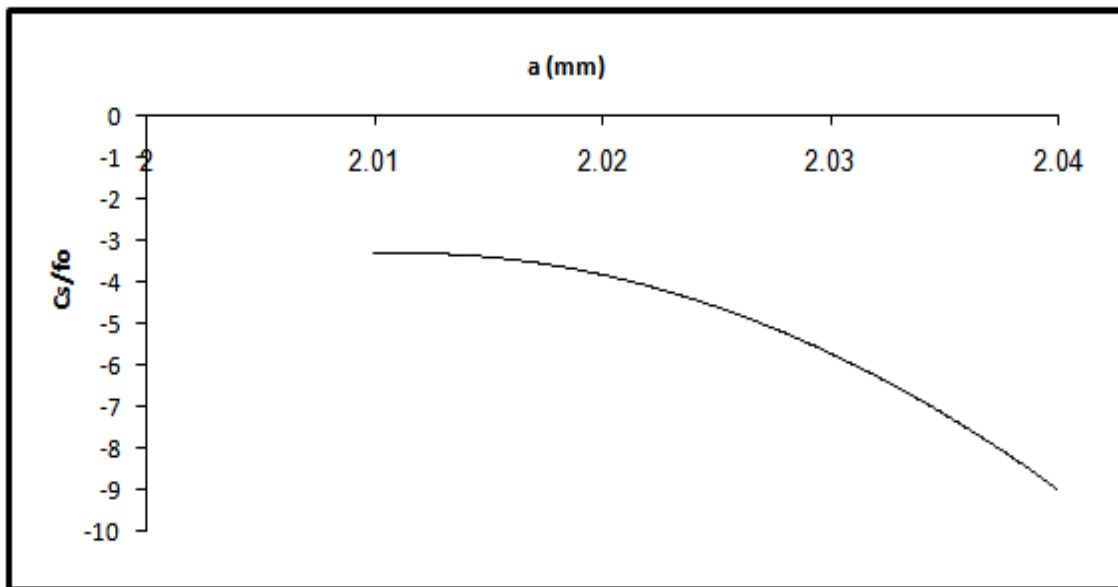

Figure (3-4): Variation of the relative spherical aberration coefficients
C_s/fo as a function of the half-width at half maximum.

3-3-1-3 chromatic aberration coefficients

The relative chromatic aberration coefficients are calculated by using Eq. (2-23), as shown in figure (3-5).
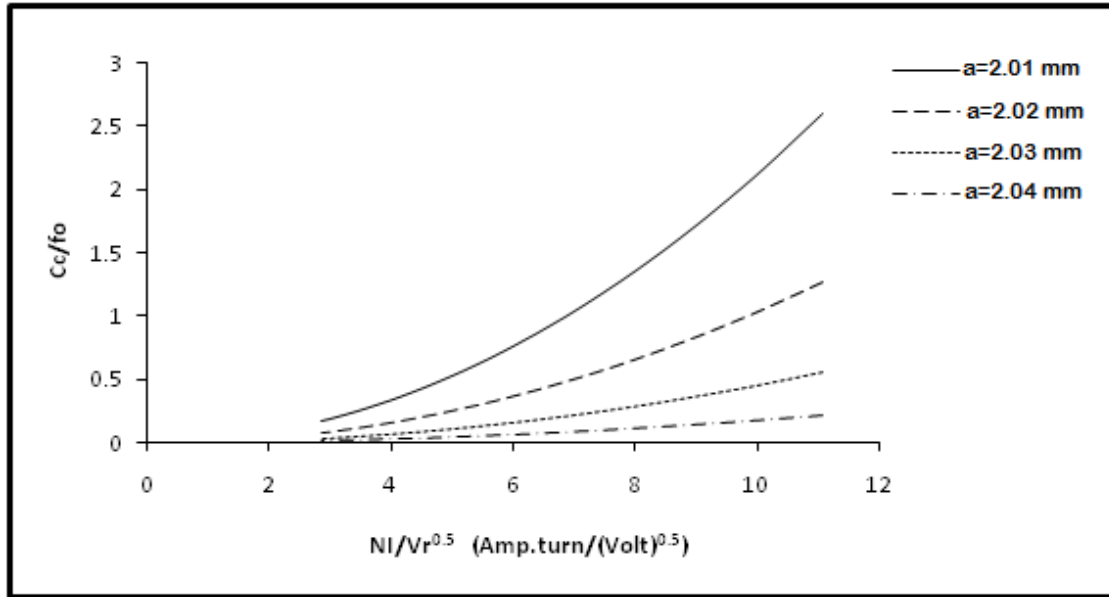

Figure (3-5): Relative chromatic aberration coefficients as a function of the excitation parameter $\left(\dfrac{NI}{\sqrt{V_r}}\right)$ for different values of the half-width at half maximum.

From this figure one can found that the values of the relative chromatic aberration coefficients C_c/fo increase as the excitation parameter $\left(\dfrac{NI}{\sqrt{V_r}}\right)$ increases. Also, the results show that the values of the relative chromatic aberration coefficients C_c/fo increase when the values of the half-width at half maximum (*a*) decrease and at the range of the half-width at half maximum (*a* = 2.01, 2.02, 2.03 and 2.04 mm) the best values of the relative chromatic aberration coefficients are found at the half-width at half maximum equal to 2.04 mm. This behavior is shown clearly in figure (3-6), where the relative chromatic aberration coefficients are plotted as a function of the half-width at half maximum for constant value of the excitation parameter $\left(\dfrac{NI}{\sqrt{V_r}}\right) = 11.068$ (Amp.turn/(Volt)$^{0.5}$).
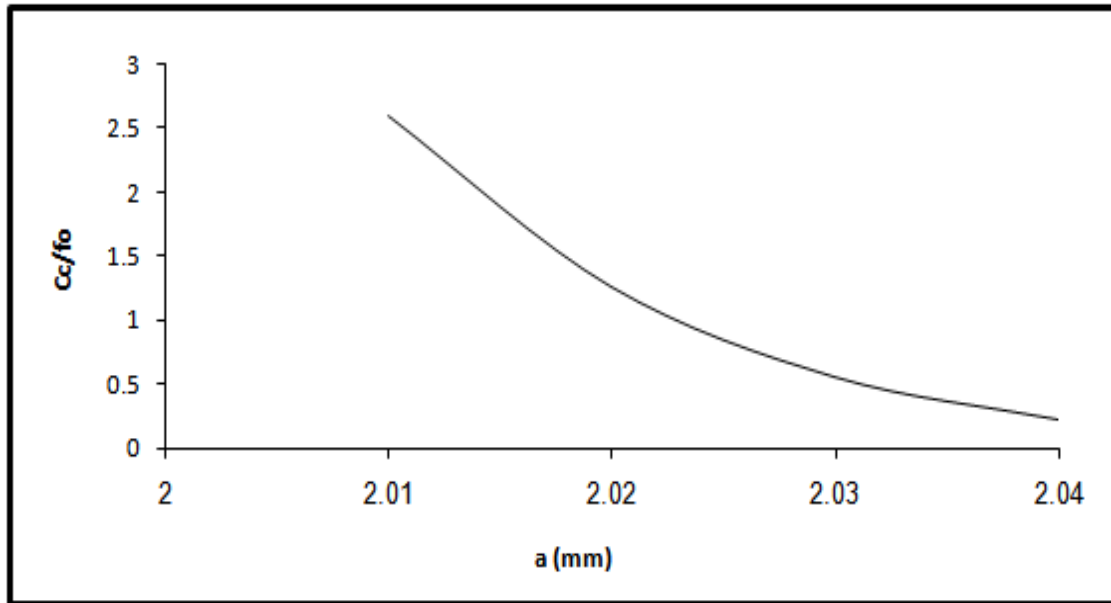
Figure (3-6): Variation of the relative chromatic aberration coefficients C_c/fo as a function of the half-width at half maximum.

3-3-1-4 spiral distortion aberration coefficients

The relative spiral aberration coefficients are computed by using Eq. (2-29), as shown in figure (3-7).
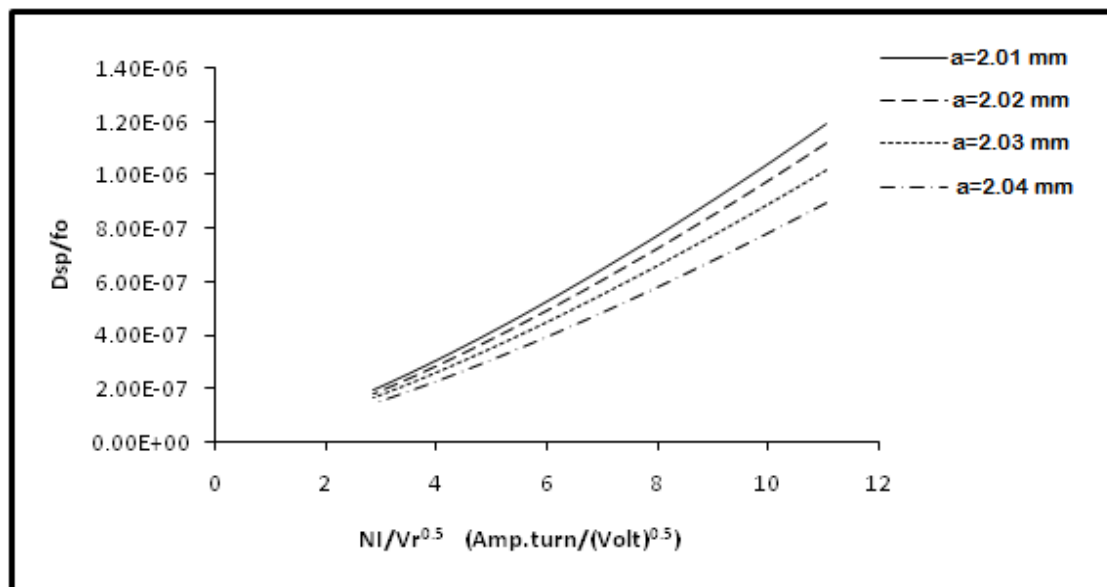

Figure (3-7): Relative spiral aberration coefficients as a function of the excitation parameter $(\frac{NI}{\sqrt{V_r}})$ for different values of the half-width at half maximum.

33

It is noticed from figure (3-7) that the values of the relative spiral aberration coefficients D_{sp}/fo increase as the excitation parameter $(\frac{NI}{\sqrt{V_r}})$ increases. Also, the results are shown that the values of the relative spiral aberration coefficients D_{sp}/fo increase when the half-width at half maximum (*a*) decrease. The minimum values of the relative spiral aberration coefficients are found at half-width at half maximum equal to 2.04 mm. This behavior is illustrated in figure (3-8), where the relative spiral aberration coefficients are plotted as a function of the half-width at half maximum for constant value of the excitation parameter $\left(\frac{NI}{\sqrt{V_r}}\right) = 11.068$ $(Amp.turn/(Volt)^{0.5})$.
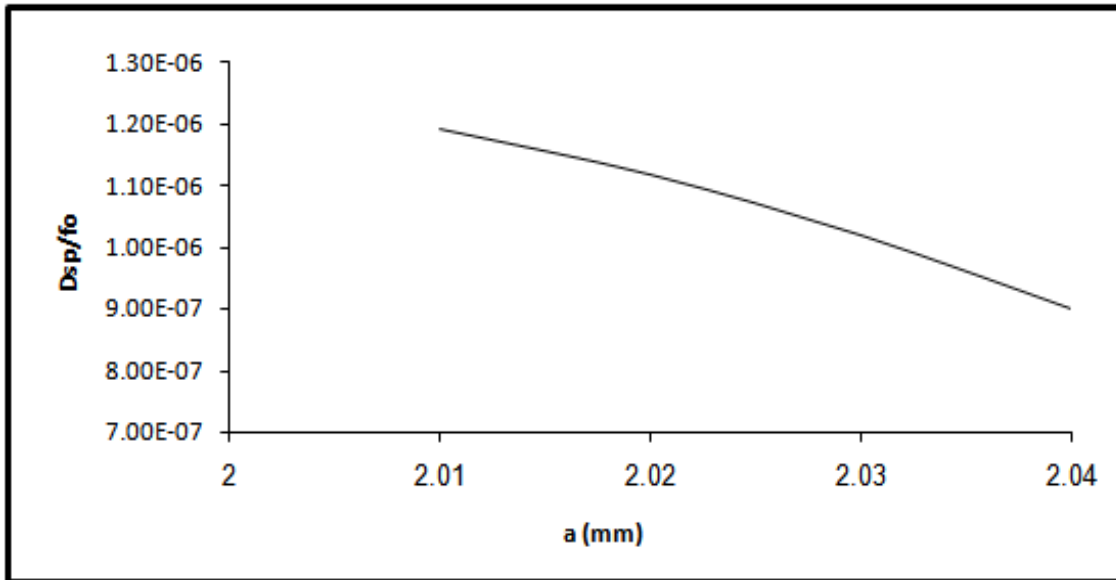

Figure (3-8): Variation of the relative spiral aberration coefficients D_{sp}/fo as a function of the half-width at half maximum.

3-3-1-5 radial distortion aberration coefficients

The relative radial aberration coefficients are computed by using Eq. (2-26) which the effects of variation of the half-width at half maximum (*a*) are studied. and the results are shown in figure (3-9).
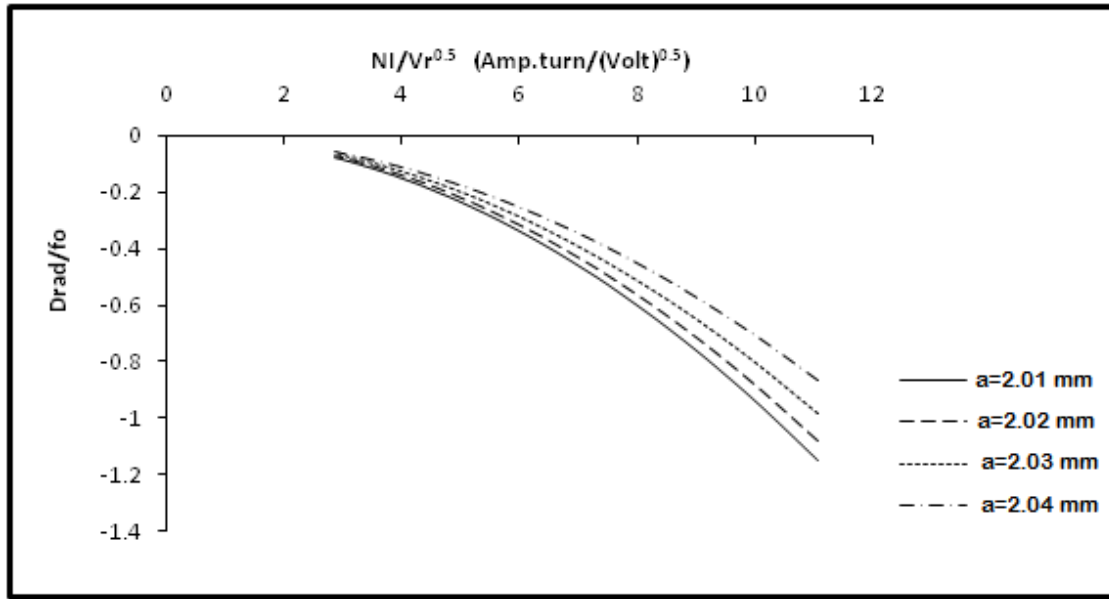
Figure (3-9): Relative radial aberration coefficients as a function of the excitation parameter $(\frac{NI}{\sqrt{V_r}})$ for different values of the half-width at half maximum.

From this figure it is noticed that the values of the relative radial distortion coefficients D_{rad}/fo decrease as the excitation parameter $(\frac{NI}{\sqrt{V_r}})$ increases. Also, the results show that the values of the relative radial distortion coefficients D_{rad}/fo increase when the half-width at half maximum (*a*) increases and at the range of the half-width at half maximum (*a* = 2.01, 2.02, 2.03 and 2.04 mm) the best values of the relative radial distortion coefficients are found at the half-width at half maximum equal to 2.01 mm. figure (3-10) illustrated the relative radial aberration coefficients as a function of the half-width at half maximum for constant value of the excitation parameter $\left(\frac{NI}{\sqrt{V_r}}\right) = 11.068$ (Amp.turn/(Volt)$^{0.5}$).
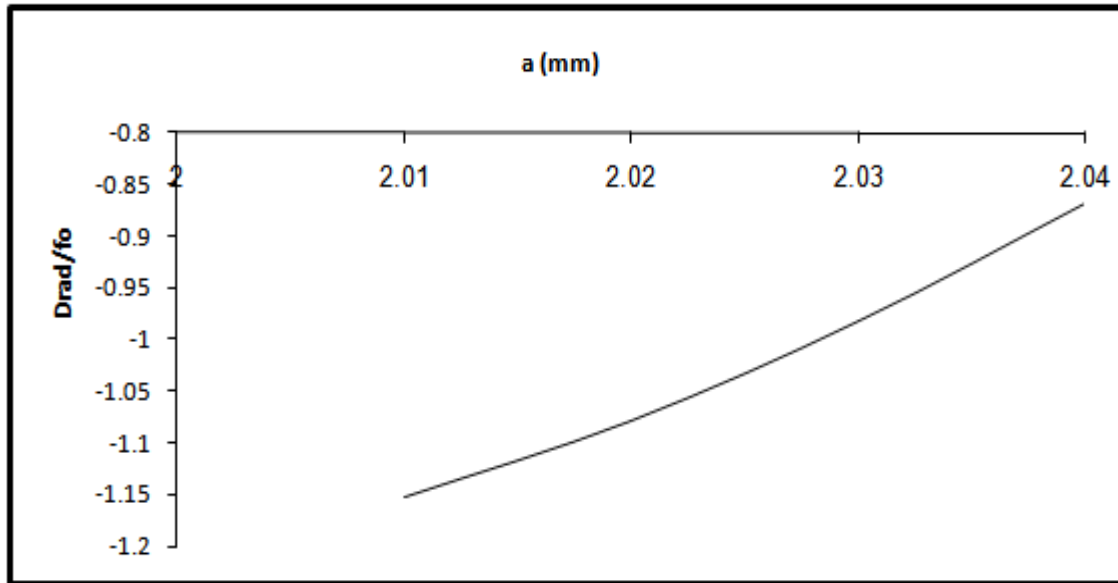
Figure (3-10): Variation of the relative radial aberration coefficients D_{rad}/fo
as a function of the half-width at half maximum.

3-3-2 The effects of changing the maximum magnetic flux density

The aberration coefficients are investigated for different values of the maximum magnetic flux density (B_m= 0.001, 0.002, 0.003 and 0.004 Tesla) at the constant value of the half-width at half maximum (a = 2.04 mm), and the results are shown as following:

3-3-2-1 spherical aberration coefficients

The relative spherical aberration coefficients are computed by using Eq. (2-20) and the effects of variation of the maximum magnetic flux density (B_m) are investigated, and the results are shown in figure (3-11).
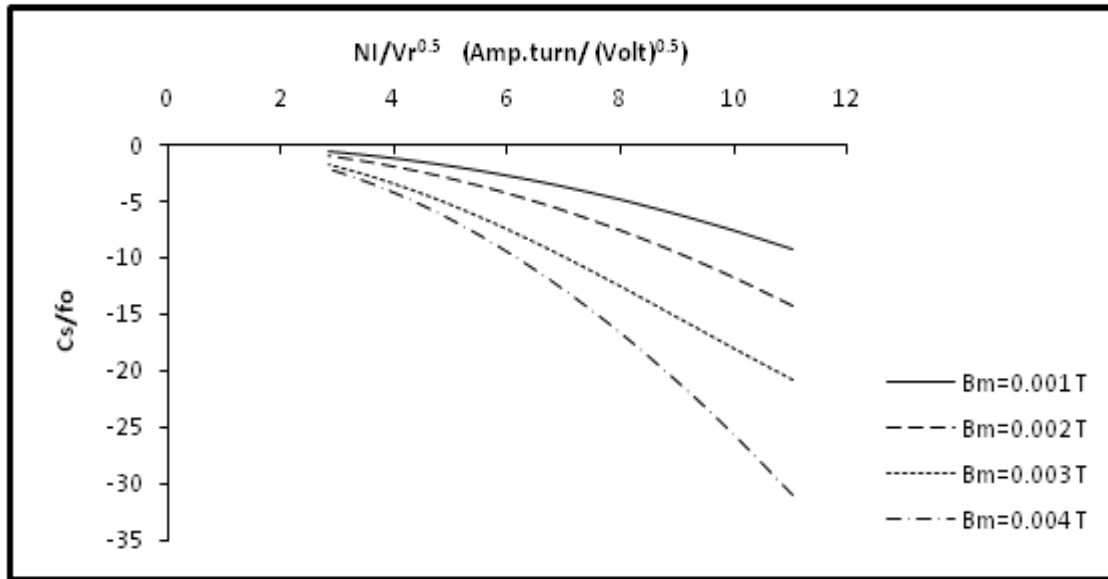
Figure (3-11): Relative spherical aberration coefficients as a function of the excitation parameter $\left(\dfrac{NI}{\sqrt{V_r}}\right)$ for different values of the maximum magnetic flux density.

From this figure one can see that the values of the relative spherical aberration coefficients C_s/fo decrease as the excitation parameter $(\dfrac{NI}{\sqrt{V_r}})$ increases.

Also, the results show that at the low values of excitation parameter $\left(\dfrac{NI}{\sqrt{V_r}}\right)$, the values of relative spherical aberration coefficients are closed to each other for different values of the maximum magnetic flux density (B_m= 0.001, 0.002 and 0.003 Tesla) and the values of the relative spherical aberration coefficients values are diverge at the range of high excitation parameter $\left(\dfrac{NI}{\sqrt{V_r}}\right)$.

In figure (3-11), the values of the relative spherical aberration coefficients C_s/fo are decreased when the maximum magnetic flux density (B_m) is increasing, and at the maximum magnetic flux density (B_m= 0.004 Tesla) one can find the best results. This behavior is shown clearly in figure (3-12), where the relative spherical aberration coefficients are plotted as a function of the maximum

magnetic flux density for constant value of the excitation parameter $\left(\frac{NI}{\sqrt{V_r}}\right) =$ 11.068 (Amp.turn/(Volt)$^{0.5}$).
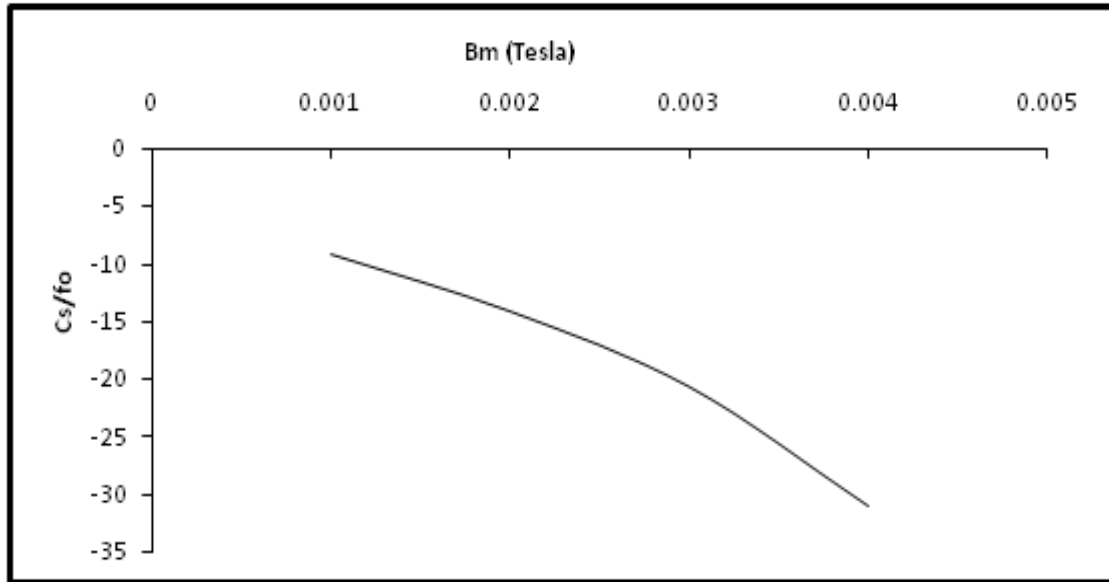

Figure (3-12): Variation of the relative spherical aberration coefficients C_s/fo as a function of the maximum magnetic flux density.

3-3-2-2 chromatic aberration coefficients

The relative chromatic aberration coefficients are calculated by using Eq. (2-23) and the effects of variation of the maximum magnetic flux density (B_m) are investigated, as shown in figure (3-13).
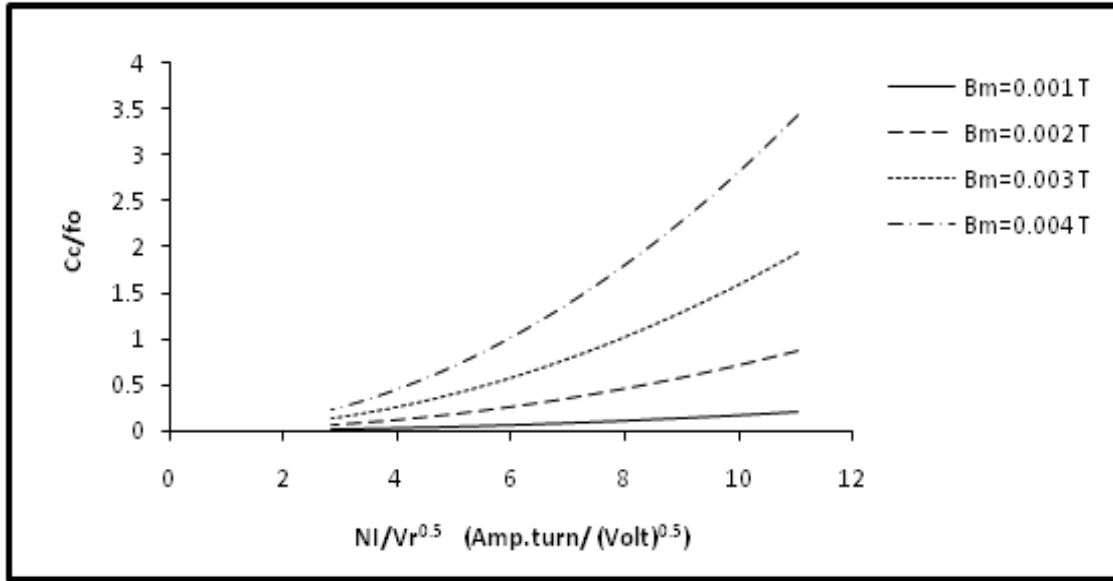
Figure (3-13): Relative chromatic aberration coefficients as a function of the excitation parameter $(\frac{NI}{\sqrt{V_r}})$ for different values of the maximum magnetic flux density.

From this figure it is founded that the values of the relative chromatic aberration coefficients C_c/fo increase as the excitation parameter $(\frac{NI}{\sqrt{V_r}})$ increases. However, the values of the relative chromatic aberration coefficients C_c/fo increase when the maximum magnetic flux density (B_m) increase, and at the range of the maximum magnetic flux density (B_m= 0.001, 0.002, 0.003 and 0.004 Tesla) the best values are found at the maximum magnetic flux density equal to 0.001 Tesla. And this behavior is shown clearly in figure (3-14), where the relative chromatic aberration coefficients are plotted as a function of the maximum magnetic flux density for constant value of the excitation parameter $\left(\frac{NI}{\sqrt{V_r}}\right) = 11.068$ (Amp.turn/(Volt)$^{0.5}$).

Figure (3-14): Variation of the relative chromatic aberration coefficients C_c /fo
as a function of the maximum magnetic flux density.

3-3-2-3 spiral distortion aberration coefficients

The relative spiral aberration coefficients are computed by using Eq. (2-29) and the effects of variation of the maximum magnetic flux density (B_m) are investigated, and the results are shown in figure (3-15).

Figure (3-15): Relative spiral aberration coefficients as a function of the
excitation parameter ($\frac{NI}{\sqrt{V_r}}$) for different values of the maximum
magnetic flux density.

It is noticed from this figure that the values of the relative spiral aberration coefficients D_{sp}/fo increase as the excitation parameter $(\frac{NI}{\sqrt{V_r}})$ increases. The values of the relative spiral aberration coefficients D_{sp}/fo increase when the maximum magnetic flux density (B_m) increase and the minimum values are found at the maximum magnetic flux density equal to 0.001 Tesla. This behavior is shown clearly in figure (3-16), where the relative spiral aberration coefficients are plotted as a function of the maximum magnetic flux density for constant value of the excitation parameter $\left(\frac{NI}{\sqrt{V_r}}\right) = 11.068$ (Amp.turn/(Volt)$^{0.5}$).
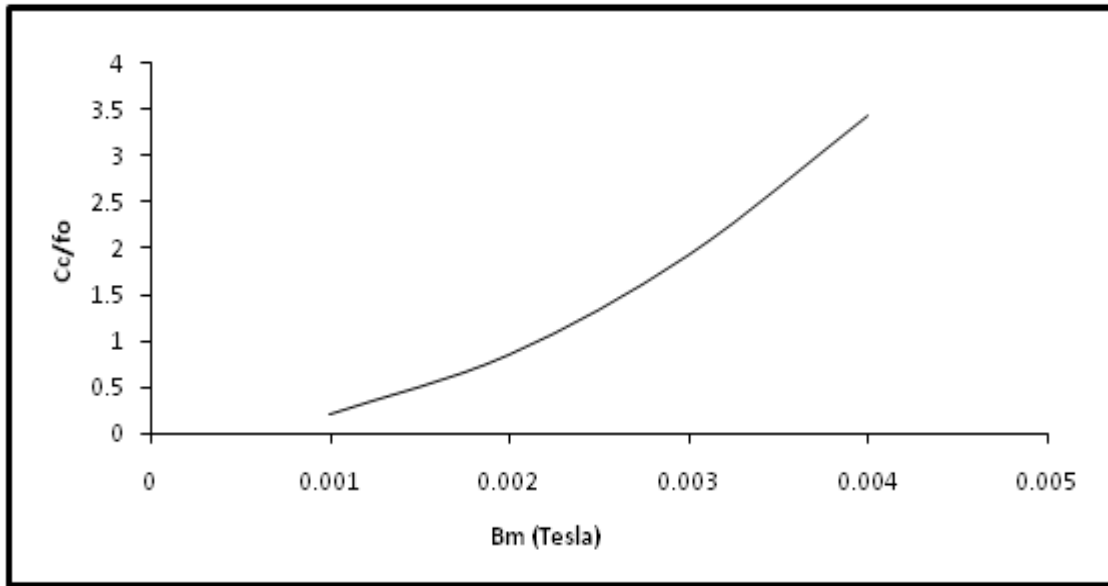

Figure (3-16): Variation of the relative spiral aberration coefficients D_{sp} /fo
        as a function of the maximum magnetic flux density.

3-3-2-4 radial distortion aberration coefficients

The relative radial aberration coefficients are estimated by using Eq. (2-26), and the effects of variation of the maximum magnetic flux density (B_m) are investigated and the results are shown in figure (3-17).
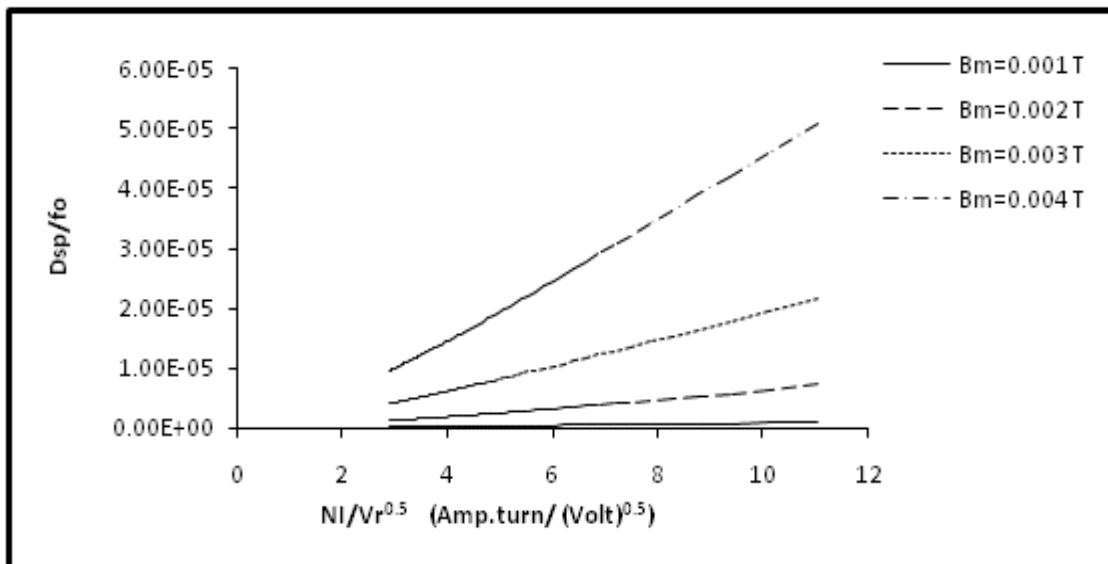
Figure (3-17): Relative radial aberration coefficients as a function of the excitation parameter $\left(\dfrac{NI}{\sqrt{V_r}}\right)$ for different values of the maximum magnetic flux density.

It is founded from figure (3-17) that the values of the relative radial aberration coefficients D_{rad}/fo decrease as the excitation parameter ($\dfrac{NI}{\sqrt{V_r}}$) increases. However, the results show that the values of the relative radial aberration coefficients D_{rad}/fo decrease when the maximum magnetic flux density (B_m) increase and at the range of the maximum magnetic flux density (B_m= 0.001, 0.002, 0.003 and 0.004 Tesla) the best values are found at the maximum magnetic flux density equal to 0.004 Tesla. This behavior is shown clearly in figure (3-18), where the relative radial aberration coefficients are plotted as a function maximum magnetic flux density for constant value of the excitation parameter $\left(\dfrac{NI}{\sqrt{V_r}}\right) = 11.068$ (Amp.turn/(Volt)$^{0.5}$).
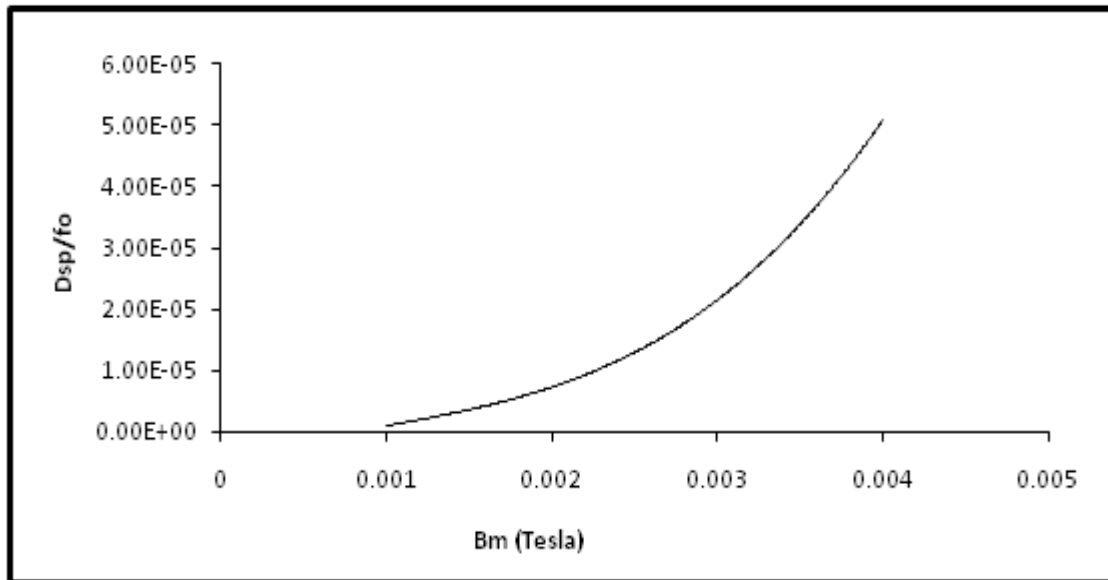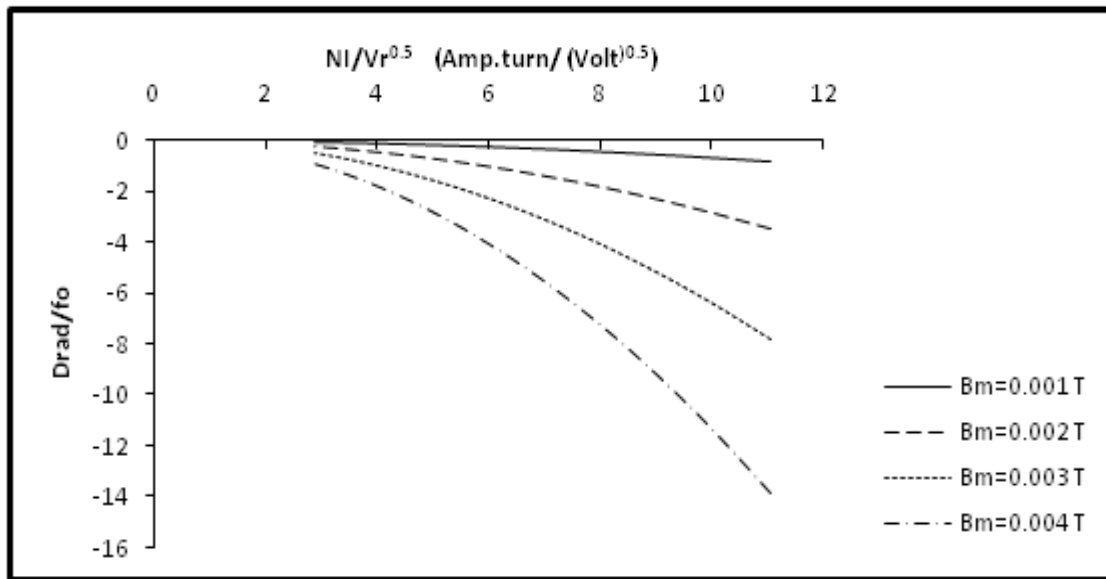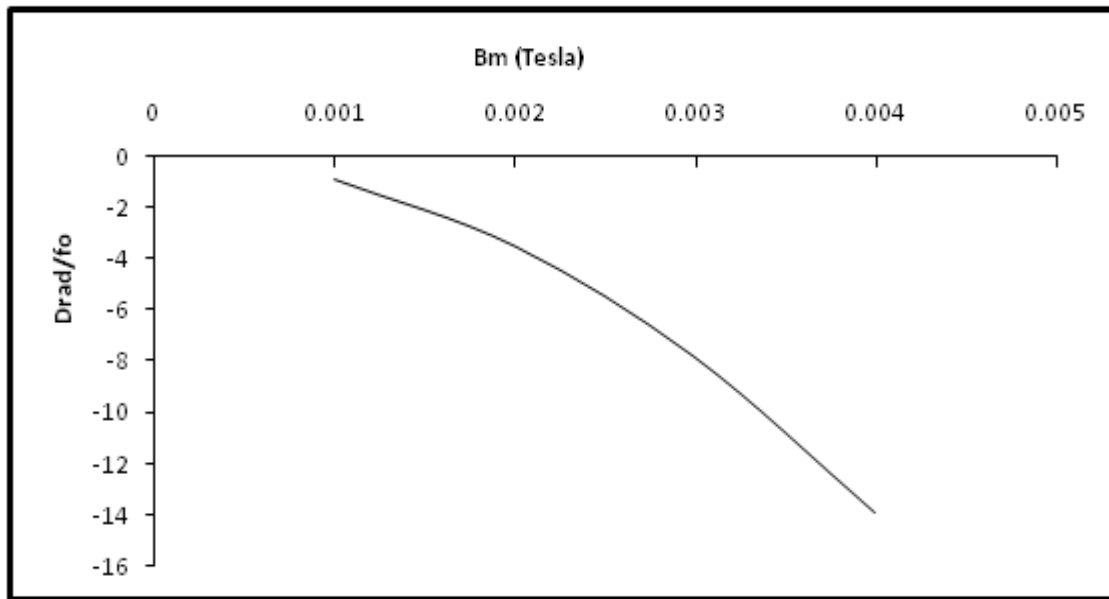
Figure (3-18): Variation of the relative radial aberration coefficients D_{rad} /fo
as a function of the maximum magnetic flux density.

The best values of the aberration coefficients are shown in table (1and 2):

Table 1: The minimum aberration coefficients for different values of the half
width at half maximum (a = 2.01, 2.02, 2.03 and 2.04 mm).

Aberration coefficients	Half width at half maximum (a)
C_s = -9.271	2.04 mm
C_c = 0.215	2.04 mm
D_{sp} = 8.99 × 10^{-7}	2.04 mm
D_{rad} = -1.152	2.01 mm

Table 2: The minimum aberration coefficients for different values of the maximum magnetic flux density (B_m = 0.001, 0.002, 0.003 and 0.004 Tesla).

Aberration coefficients	Maximum magnetic flux density ($B_{m)}$
C_s = -3.136	0.004 Tesla
C_c = 0.215	0.001 Tesla
D_{sp} = 8.9 × 10^{-7}	0.001 Tesla
D_{rad} = -13.889	0.004 Tesla

3-4 Non-Zero Initial Momentum

3-4-1 The effects of changing the electron emission angle

The aberration coefficients are computed for different values of the electron emission angle (θ = 0.2, 0.4, 0.5 and 0.6 rad) at constant maximum magnetic flux density (B_m = 0.006 Tesla) and constant value of the half-width at half maximum (a = 2.01 mm), and the results are as following:

3-4-1-1 electron beam trajectory

The analytical solution can be obtained for r/r_o for equation (2-5) with Glaser's field, since the adjacent trajectories with different values of the angular component of the momentum p_θ has been taken into account. The electron beam trajectory along the magnetic field has been computed using Eq. (2-12), and the effects of changing the electron emission angle has been investigation at constant value of the excitation parameter ($\frac{NI}{\sqrt{V_r}}$) =11.068 (Amp.turn/(Volt)$^{0.5}$), and the results are shown in figure (3-19).
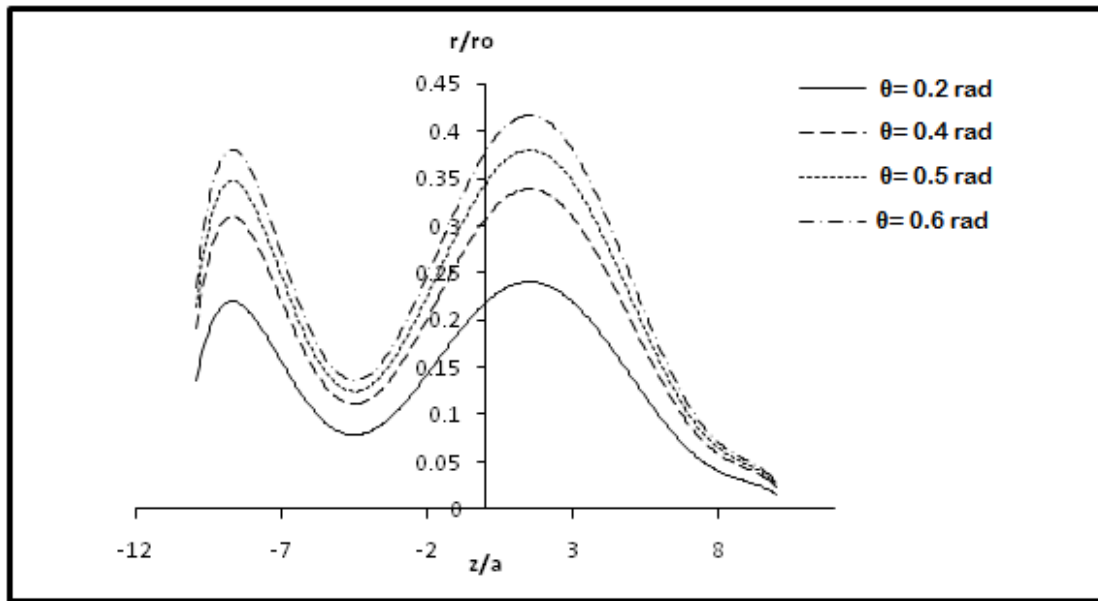
Figure (3-19): Electron beam trajectory for the magnetic lens at excitation parameter $\left(\dfrac{NI}{\sqrt{V_r}}\right)= 11.068(Amp.turn/(Volt)^{0.5})$ for different values of the electron emission angles.

The computations appear that when the values of the electron emission angle (θ) decrease the electron beam trajectory becomes more smooth , i.e. the fluctuation between the upper and lower values of the displacement from the optical axis reduce.

The variation between the upper and lower values of r/r_o of the trajectory for whole range of the relative optical path z/a is increasing when the electron emission angle (θ) increase.

3-4-1-2 spherical aberration coefficients

The relative spherical aberration coefficients are calculated for different values of the electron emission angle, and the results are shown in figure (3-20).

Figure (3-20): Relative spherical aberration coefficients as a function of the excitation parameter $\left(\frac{NI}{\sqrt{V_r}}\right)$ for different values of the electron emission angle.

From this figure one can observed that at the low values of excitation parameter $\left(\frac{NI}{\sqrt{V_r}}\right)$ the values of the relative spherical aberration coefficients are closed to each other for different values of the electron emission angles, and the relative spherical aberration coefficients values diverge at the range of high excitation parameter $\left(\frac{NI}{\sqrt{V_r}}\right)$. The values of the relative spherical aberration coefficients C_s/fo decrease when the electron emission angle (θ) increase and at the electron emission angle equal to 0.6 rad one can find the lowest values of the relative spherical aberration coefficients. This behavior is shown clearly in figure (3-21), where the relative spherical aberration coefficients are plotted as a function of the electron emission angle at constant value of the excitation parameter $\left(\frac{NI}{\sqrt{V_r}}\right) = 11.068$ (Amp.turn/(Volt)$^{0.5}$).
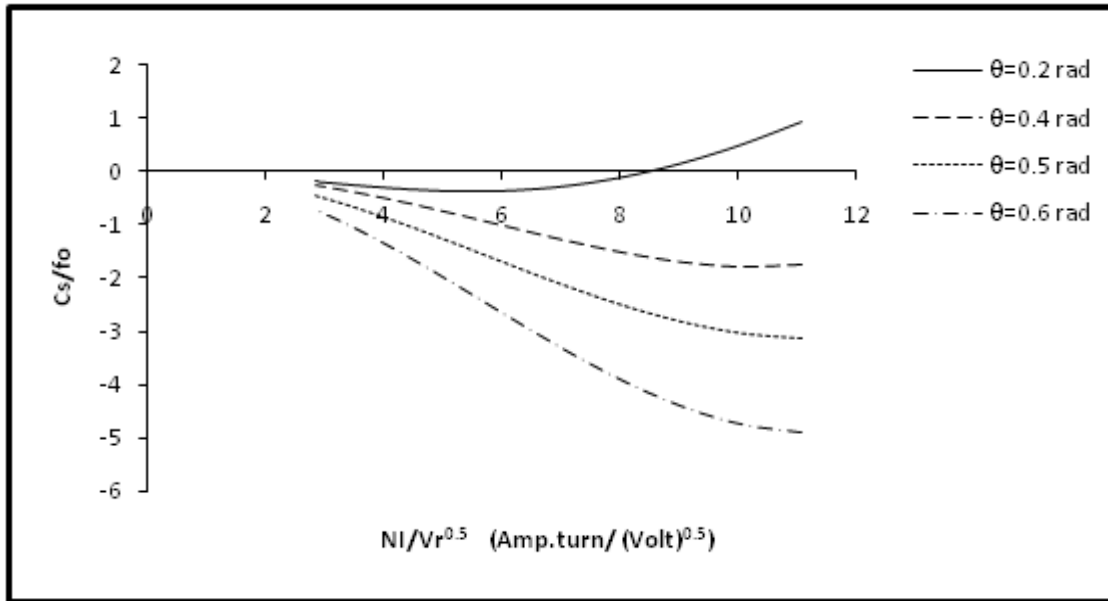
Figure (3-21): Variation of the relative spherical aberration coefficients C_s/fo
as a function of the electron emission angle.

3-4-1-3 chromatic aberration coefficients

The relative chromatic aberration coefficients are calculated for different values of the electron emission angle, and the results are shown in figure (3-22).

Figure (3-22): Relative chromatic aberration coefficients as a function of
the excitation parameter $(\frac{NI}{\sqrt{V_r}})$ for different values of the electron
emission angle.

From this figure one can find that the values of the relative chromatic aberration coefficients C_c/fo increase as the excitation parameter $(\frac{NI}{\sqrt{V_r}})$ increases. The relative chromatic aberration coefficients C_c/fo has minimum value at the electron emission angle equal to 0.2 rad. From these results one can be observed that the increasing of the electron emission angle leads to increase the relative chromatic aberration coefficients. In figure (3-23), the relative chromatic aberration coefficients are plotted as a function of the electron emission angle at constant value of the excitation parameter $\left(\frac{NI}{\sqrt{V_r}}\right) = 11.068$ (Amp.turn/(Volt)$^{0.5}$).
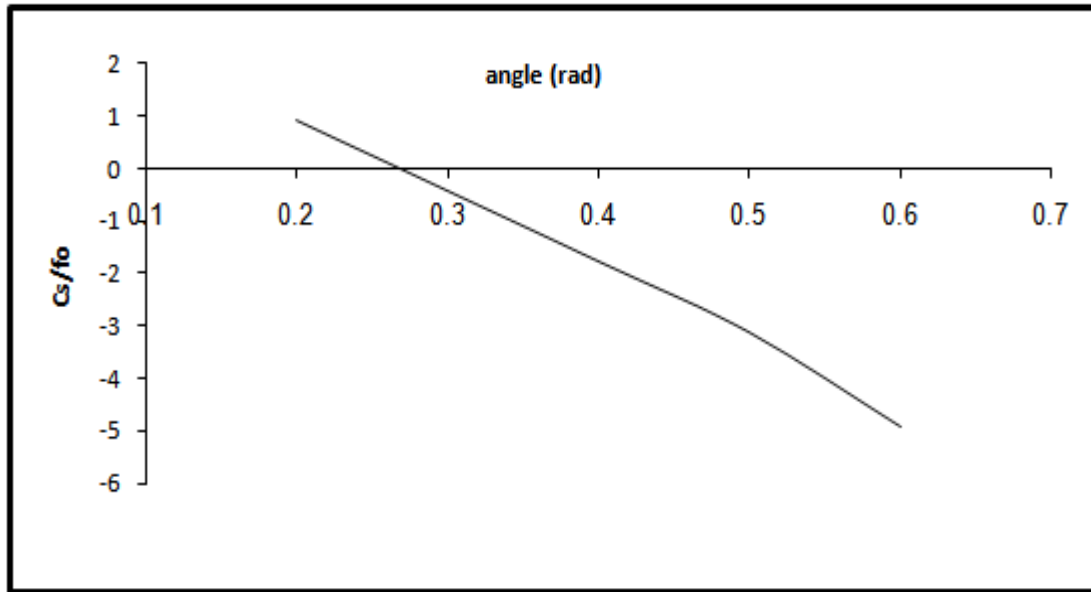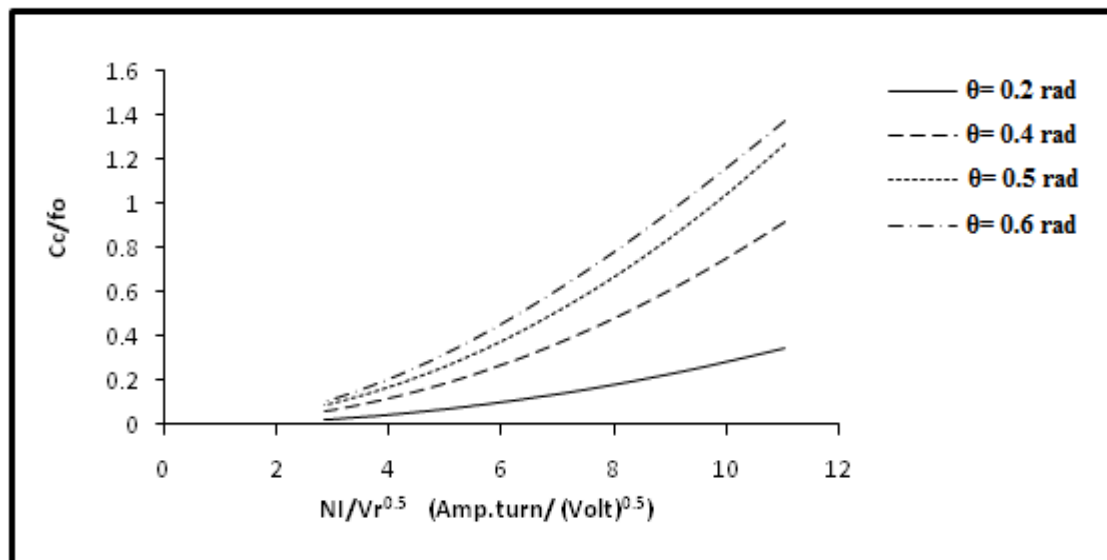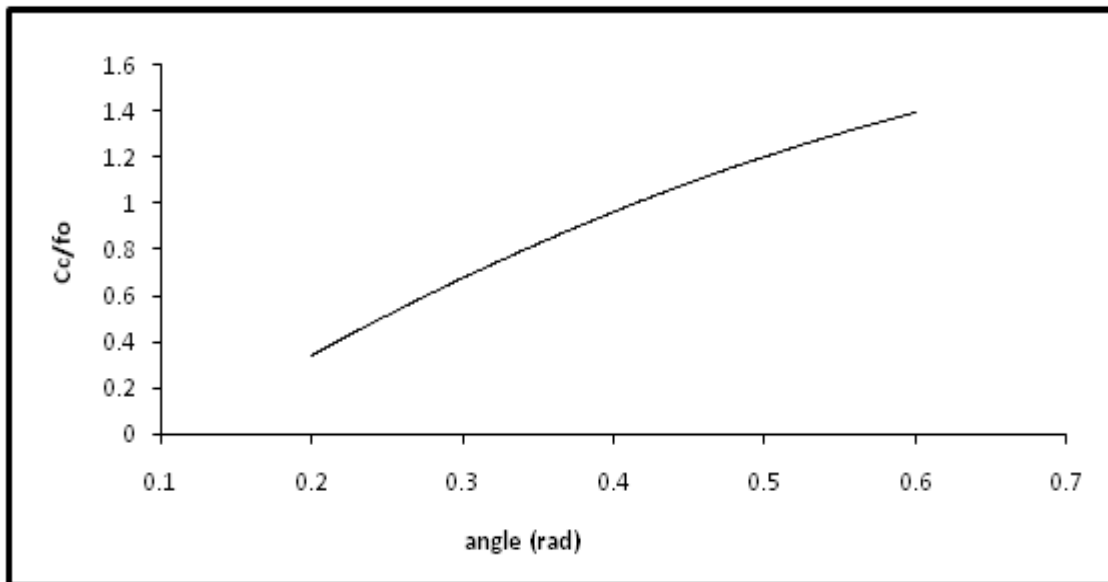

Figure (3-23): Variation of the relative chromatic aberration coefficients
C_c/fo as a function of the electron emission angle.

3-4-1-4 spiral distortion aberration coefficients

The relative spiral aberration coefficients are calculated for different values of the electron emission angle, and the results are shown in figure (3-24).

Figure (3-24): Relative spiral aberration coefficients as a function of the excitation parameter $\left(\frac{NI}{\sqrt{V_r}}\right)$ for different values of the electron emission angle.

From this figure one can find that the values of the relative spiral aberration coefficients C_c/fo increase as the excitation parameter $(\frac{NI}{\sqrt{V_r}})$ increases. Also the relative spiral aberration coefficients C_c/fo has best value at the electron emission angle equal to 0.2 rad. From these results one can observed that the increasing of the electron emission angle leads to increase the relative spiral aberration coefficients. This behavior is shown clearly in figure (3-25), where the relative spiral aberration coefficients are plotted as a function of the electron emission angle at constant value of the excitation parameter $\left(\frac{NI}{\sqrt{V_r}}\right) = 11.068$ (Amp.turn/(Volt)$^{0.5}$).

Figure (3-25): Variation of the relative spiral aberration coefficients D_{sp} /fo as
a function of the electron emission angle.

3-4-1-5 radial distortion aberration coefficients

The relative radial aberration coefficients are found for different values of the
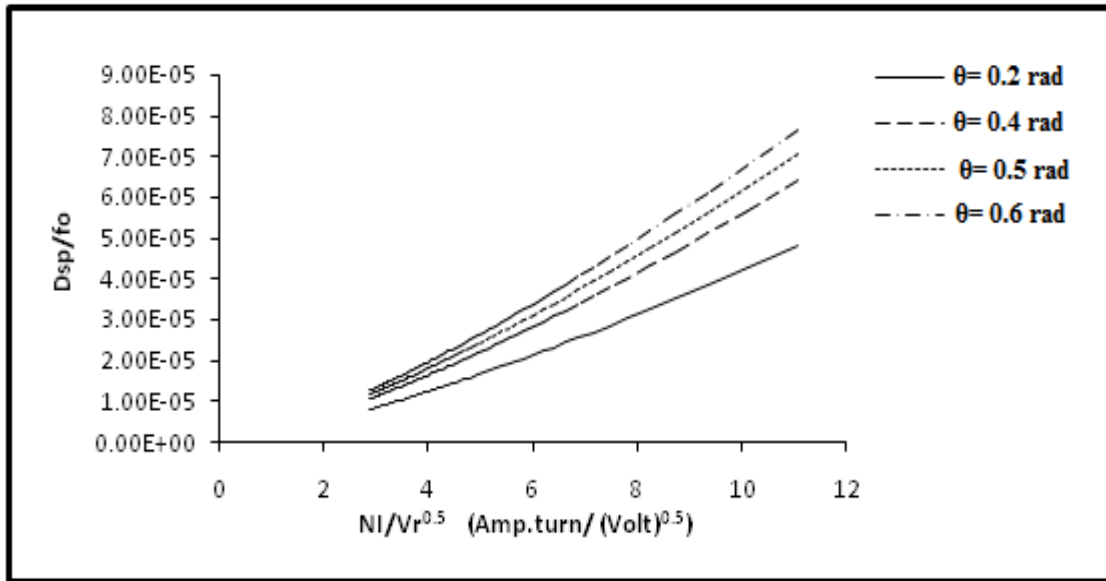electron emission angles, and the results are shown in figure (3-26).

Figure (3-26): Relative radial aberration coefficients as a function of the
excitation parameter $\left(\dfrac{NI}{\sqrt{V_r}} \right)$ for different values of the electron
emission angle.

Figure (3-26) shows that the relative radial aberration coefficients D_{rad}/fo decrease as the excitation parameter $(\frac{NI}{\sqrt{V_r}})$ increases. Also the relative radial aberration coefficients C_c/fo at the range of the electron emission angle ($\theta = 0.2$, 0.4, 0.5 and 0.6 rad) has optimum value at the electron emission angle equal to 0.6 rad. From these results one can observed that the increasing of the electron emission angle leads to decrease the relative radial aberration coefficients. This behavior is shown clearly in figure (3-27), where the relative radial aberration coefficients are plotted as a function of the electron emission angle at constant value of the excitation parameter $\left(\frac{NI}{\sqrt{V_r}}\right) = 11.068$ (Amp.turn/(Volt)$^{0.5}$).
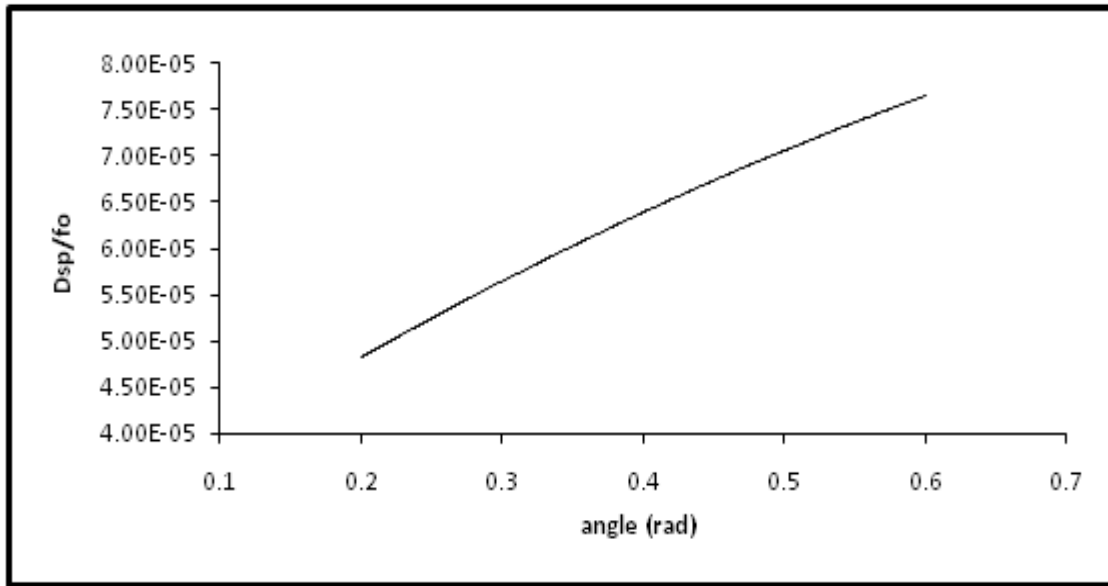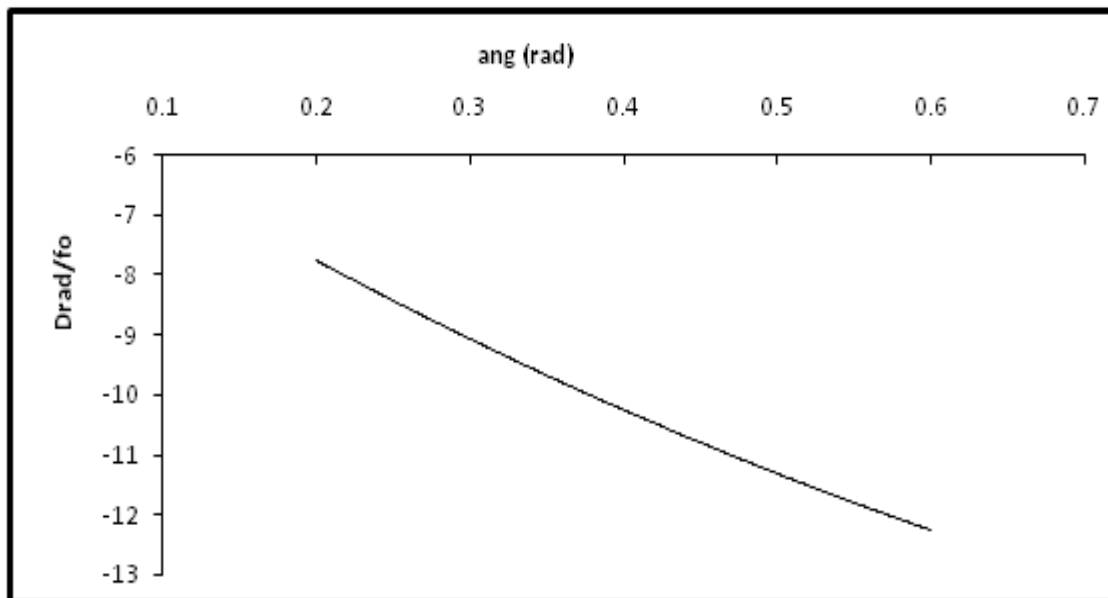

Figure (3-27): Variation of the relative radial aberration coefficients D_{rad} /fo
as a function of the electron emission angle.

The best values of the aberration coefficients are shown in tables (3, 4 and 5):

Table 3: The minimum aberration coefficients for different values of the
electron emission angles (θ =0.2, 0.4, 0.5 and 0.6 rad).

Aberration coefficients	Electron emission angle (θ)
C_s = -4.918	0.6 rad
C_c = 0.346	0.2 rad
D_{sp} = 4.83 × 10^{-5}	0.2 rad
D_{rad} = -12.265	0.6 rad

3-4-2 The effects of changing the half-width at half maximum

The aberration coefficients are computed for different values of the half-width at half maximum (a = 2.01, 2.02, 2.03 and 2.04 mm) at constant maximum magnetic flux density (B_m = 0.006 Tesla) and constant value of the electron emission angle (θ = 0.2 rad), and the results are shown as following:

3-4-2-1 spherical aberration coefficients

The relative spherical aberration coefficients are calculated for different values of the half-width at half maximum, and the results are shown in figure (3-28).
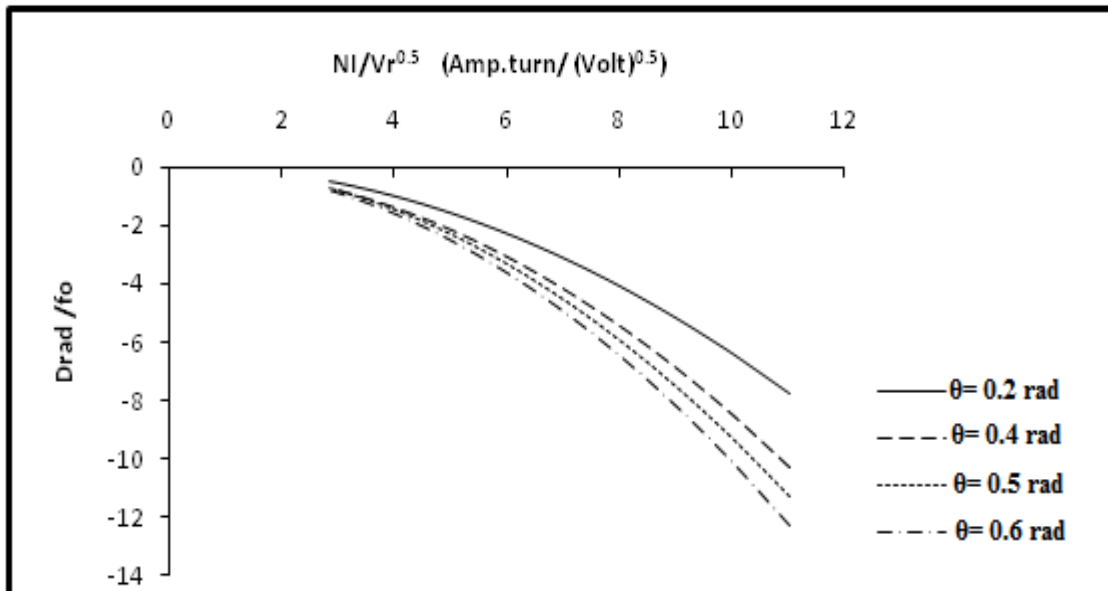
Figure (3-28): Relative spherical aberration coefficients as a function of the excitation parameter $\left(\frac{NI}{\sqrt{V_r}}\right)$ for different values of the half-width at half maximum.

From this figure one can observed that at the low values of excitation parameter $(\frac{NI}{\sqrt{V_r}})$ the values of the relative spherical aberration coefficients are closed to each other for different values of the half-width at half maximum, and the relative spherical aberration coefficients take the negative values up to excitation parameter $\left(\frac{NI}{\sqrt{V_r}}\right)$ equal to 8.5.

Also, the values of the relative spherical aberration coefficients C_s/fo decrease when the half-width at half maximum (*a*) increase, and at the half-width at half maximum equal to 2.04 mm one can find the lowest values, but this behavior is true up to excitation parameter $\left(\frac{NI}{\sqrt{V_r}}\right)$ equal to 8.5, and the opposite behavior occurs for high values of the excitation parameter.

3-4-2-2 chromatic aberration coefficients

The relative chromatic aberration coefficients C_c/fo have been computed for different values of the half-width at half maximum and the results are shown in figure (3-29).
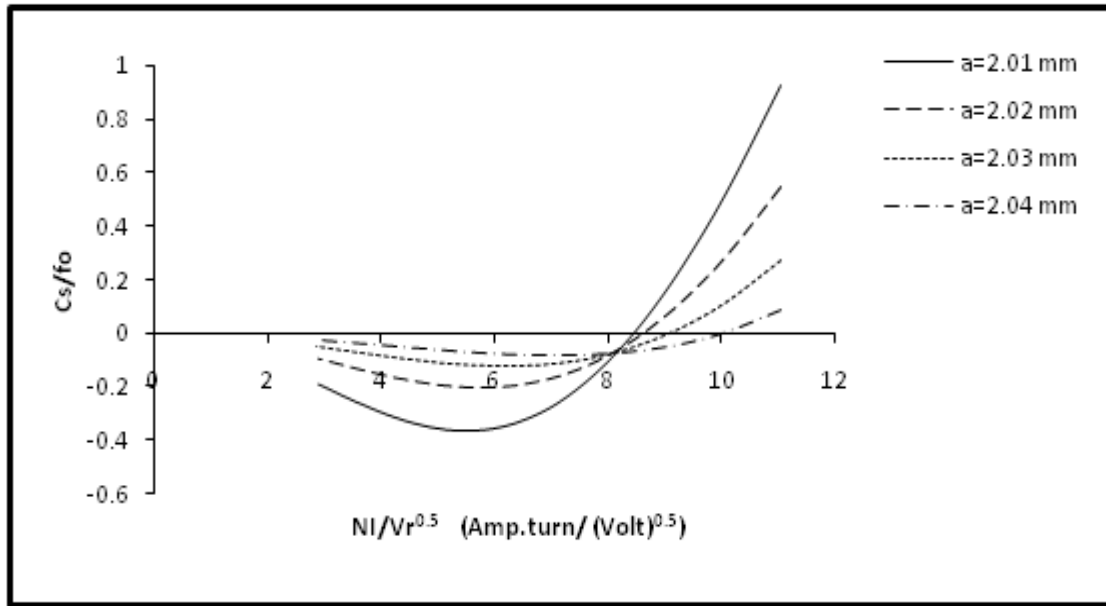

Figure (3-29): Relative chromatic aberration coefficients as a function of the excitation parameter $\left(\dfrac{NI}{\sqrt{V_r}}\right)$ for different values of the half-width at half maximum.

This figure appears that the values of the relative chromatic aberration coefficients C_c/fo increase as the excitation parameter $(\dfrac{NI}{\sqrt{V_r}})$ increases. Also, the results show that the values of the relative chromatic aberration coefficients C_c/fo decrease when the values of the half-width at half maximum (*a*) increase, and at the range of the half-width at half maximum (*a* = 2.01, 2.02, 2.03 and 2.04 mm) the lowest values of the relative chromatic aberration coefficients are found at the half-width at half maximum equal to 2.04 mm

3-4-2-3 spiral distortion aberration coefficients

The relative spiral aberration coefficients have been computed for different values of the half-width at half maximum and the results are shown in figure (3-30).

Figure (3-30): Relative spiral aberration coefficients as a function of the excitation parameter $\left(\dfrac{NI}{\sqrt{V_r}}\right)$ for different values of the half-width at half maximum.

From this figure one can find that the values of the relative spiral aberration coefficients D_{sp}/fo increase as the excitation parameter $(\dfrac{NI}{\sqrt{V_r}})$ increases. Also, the results show that the values of the relative spiral aberration coefficients D_{sp}/fo decrease when the half-width at half maximum (*a*) increase. The lowest values of the relative spiral aberration coefficients are found at half-width at half maximum equal to 2.04 mm.

3-4-2-4 radial distortion aberration coefficients

The relative radial aberration coefficients have been computed for different values of the half-width at half maximum and the results are shown in figure (3-31).

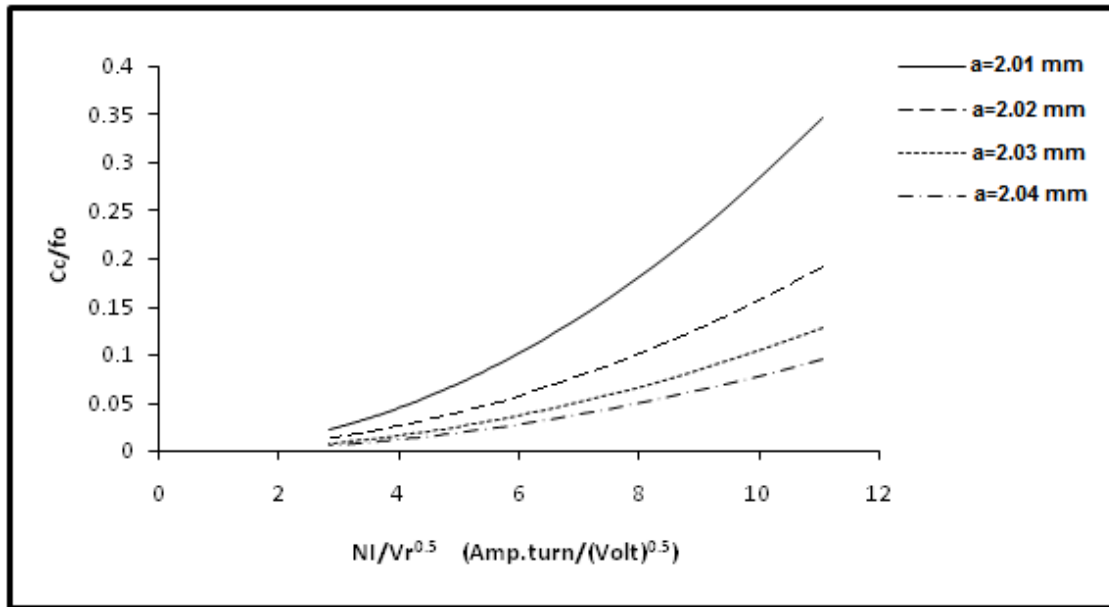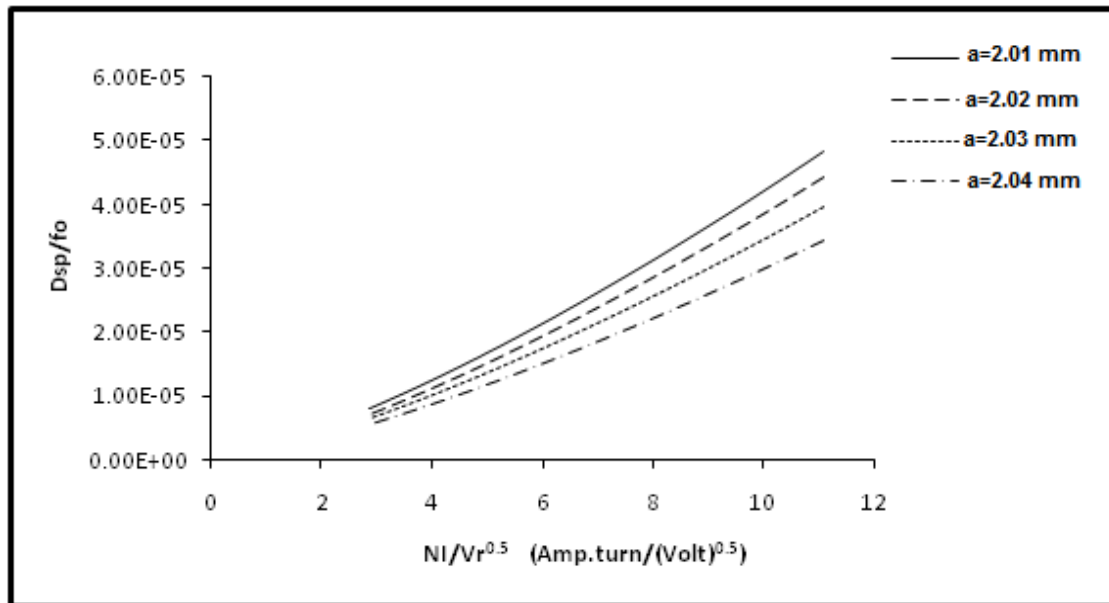Figure (3-31): Relative radial aberration coefficients as a function of the excitation parameter $\left(\dfrac{NI}{\sqrt{V_r}}\right)$ for different values of the half-width at half maximum.

From this figure one can find that the values of the relative radial distortion coefficients D_{rad}/fo decrease as the excitation parameter $(\dfrac{NI}{\sqrt{V_r}})$ increases. Also, the results show that the values of the relative radial distortion coefficients D_{rad}/fo increase when the half-width at half maximum (*a*) increases and at the range of the half-width at half maximum (*a* = 2.01, 2.02, 2.03 and 2.04 mm) the best values of the relative radial distortion coefficients are found at the half-width at half maximum equal to 2.01 mm.

Table 4: The minimum aberration coefficients for different values of the half width at half maximum (a = 2.01, 2.02, 2.03 and 2.04 mm).

Aberration coefficients	Half width at half maximum (a)
C_s = -0.087	2.04 mm
C_c = 0.095	2.04 mm

$D_{sp} = 3.44 \times 10^{-5}$	2.04 mm
$D_{rad} = -7.747$	2.01 mm

3-4-3 The effects of changing the maximum magnetic flux density

The aberration coefficients are computed for different values of the maximum magnetic flux density (B_m= 0.002, 0.003, 0.004 and 0.006 Tesla) at constant value of the half-width at half maximum (a = 2.01 mm) and constant value of the electron emission angle (θ = 0.2 rad) and the results are shown as following:

3-4-3-1 spherical aberration coefficients

The relative spherical aberration coefficients are calculated for different values of the maximum magnetic flux density, and the results are shown in figure (3-32).
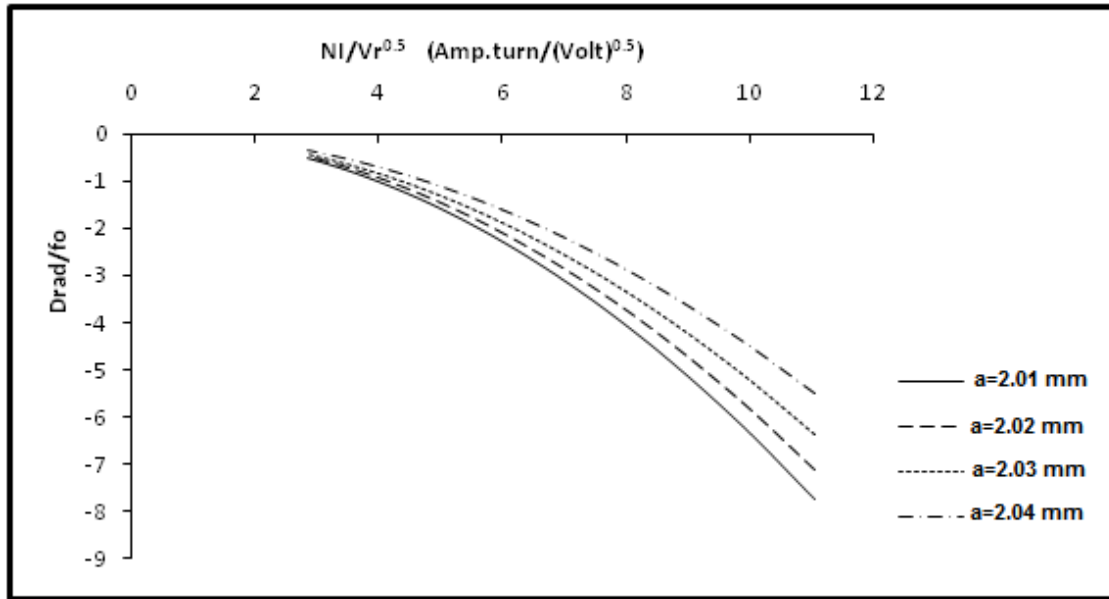

Figure (3-32): Relative spherical aberration coefficients as a function of the excitation parameter ($\frac{NI}{\sqrt{V_r}}$)for different values of the maximum magnetic flux density.

From this figure one can find that the values of the relative spherical aberration coefficients C_s/fo increase as the excitation parameter $(\frac{NI}{\sqrt{V_r}})$ increases. The results show that the values of the spherical aberration coefficients are negative and these results can be used to design the magnetic lens which can be achieved the role of the corrector in the electron optical system.

In figure (3-32), the values of the relative spherical aberration coefficients C_s/fo increase when the maximum magnetic flux density (B_m) is increasing, and at the maximum magnetic flux density equal to B_m= 0.002 one can find the best results.

3-4-3-2 chromatic aberration coefficients

The relative chromatic aberration coefficients C_c/fo are calculated for different values of the maximum magnetic flux density, the results are show in figure (3-33).

Figure (3-33): Relative chromatic aberration coefficients as a function of the excitation parameter $\left(\frac{NI}{\sqrt{V_r}}\right)$ for different values of the maximum magnetic flux density.

From this figure one can find that the values of the relative chromatic aberration coefficients C_c/fo increase as the excitation parameter $(\frac{NI}{\sqrt{V_r}})$ increases. Also, the

results show that the values of relative chromatic aberration coefficients C_c/fo increase when the maximum magnetic flux density (B_m) increase, and at the range of the maximum magnetic flux density (B_m= 0.002, 0.003, 0.004 and 0.006 Tesla) the best values are found at the maximum magnetic flux density equal to 0.002 Tesla.

3-4-3-3 spiral distortion aberration coefficients

The relative spiral aberration coefficients are computed for different values of the maximum magnetic flux density and the results are shown in fig (3-34).
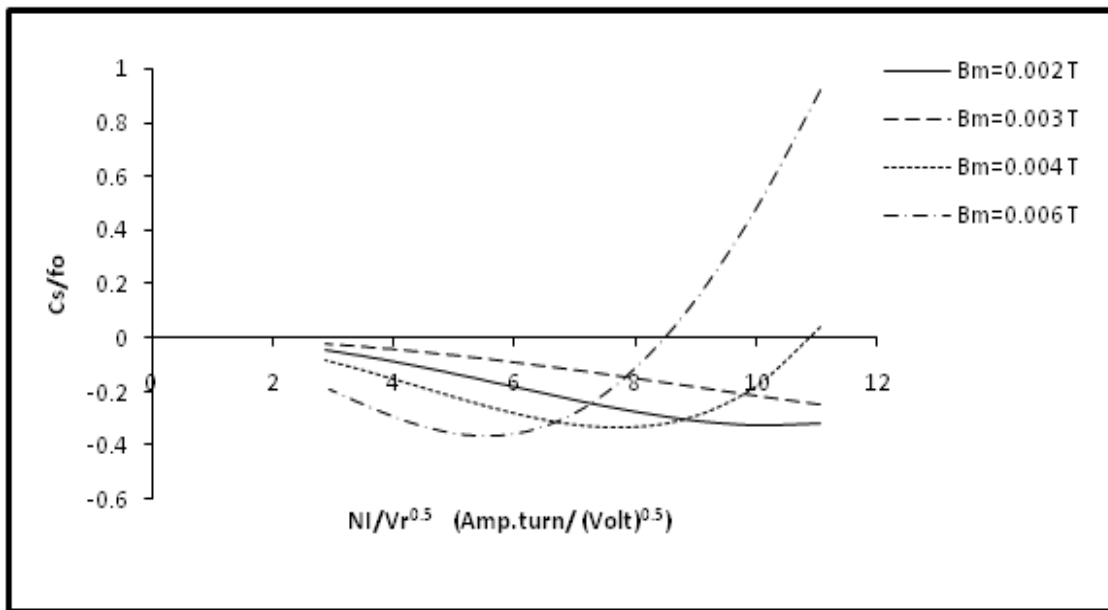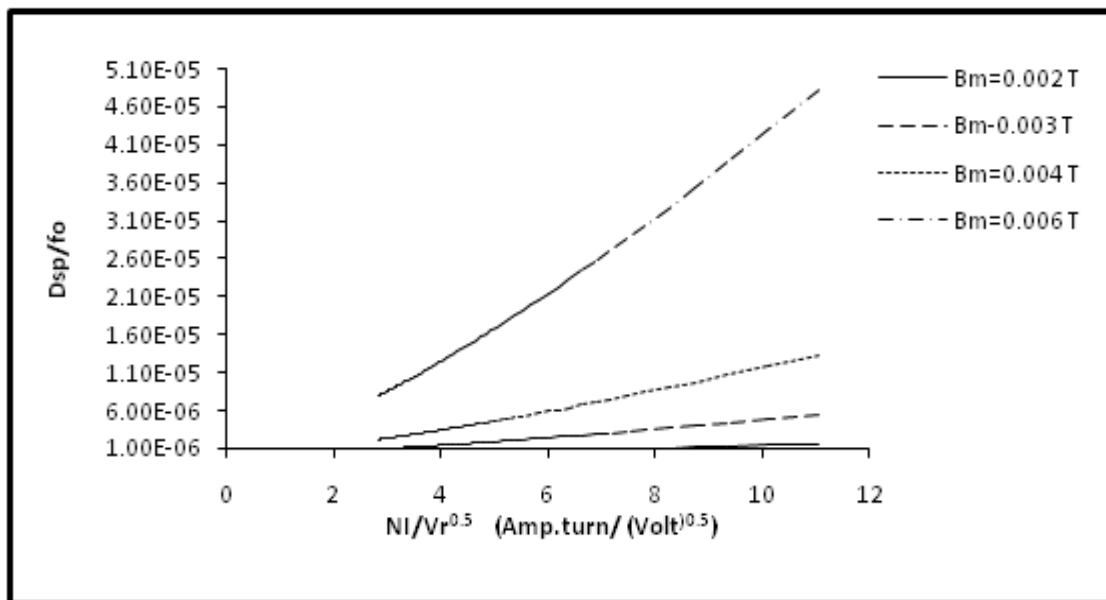

Figure (3-34): Relative spiral aberration coefficients as a function of the excitation parameter $(\frac{NI}{\sqrt{V_r}})$ for different values of the maximum magnetic flux density.

From this figure one can find that the values of the relative spiral aberration coefficients D_{sp}/fo increase as the excitation parameter $(\frac{NI}{\sqrt{V_r}})$ increases. Also, the results show that the values of the relative spiral   aberration coefficients D_{sp}/fo increase when the maximum magnetic flux density (B_m) increase and the minimum values are found at the maximum magnetic flux density equal to 0.002 Tesla.

3-4-3-4 radial distortion aberration coefficients

The relative radial aberration coefficients have been computed for different values of the maximum magnetic flux density, and the results are shown in figure (3-35).
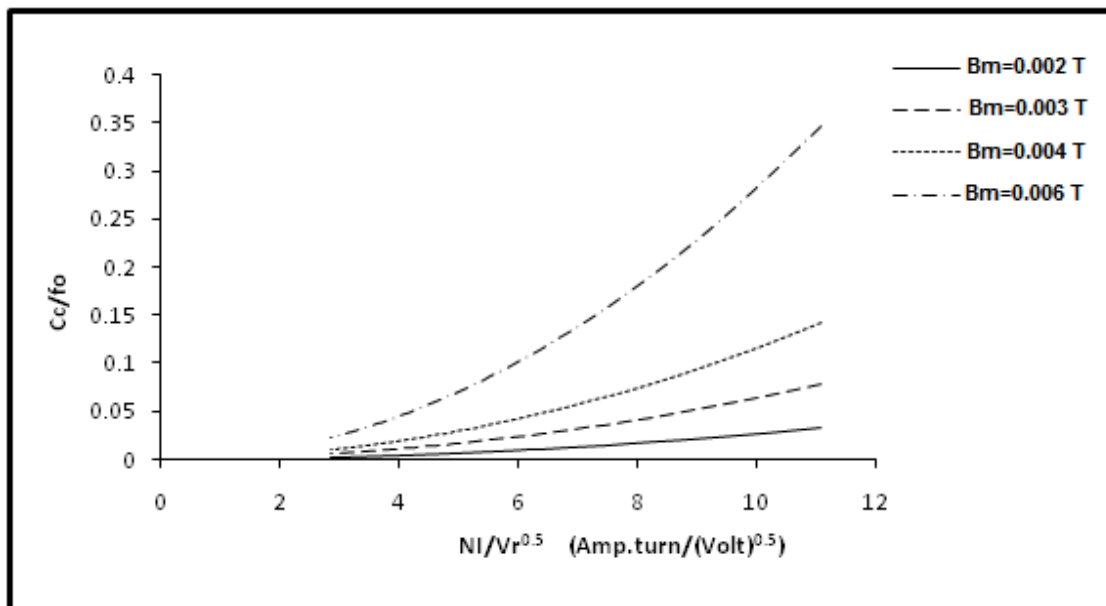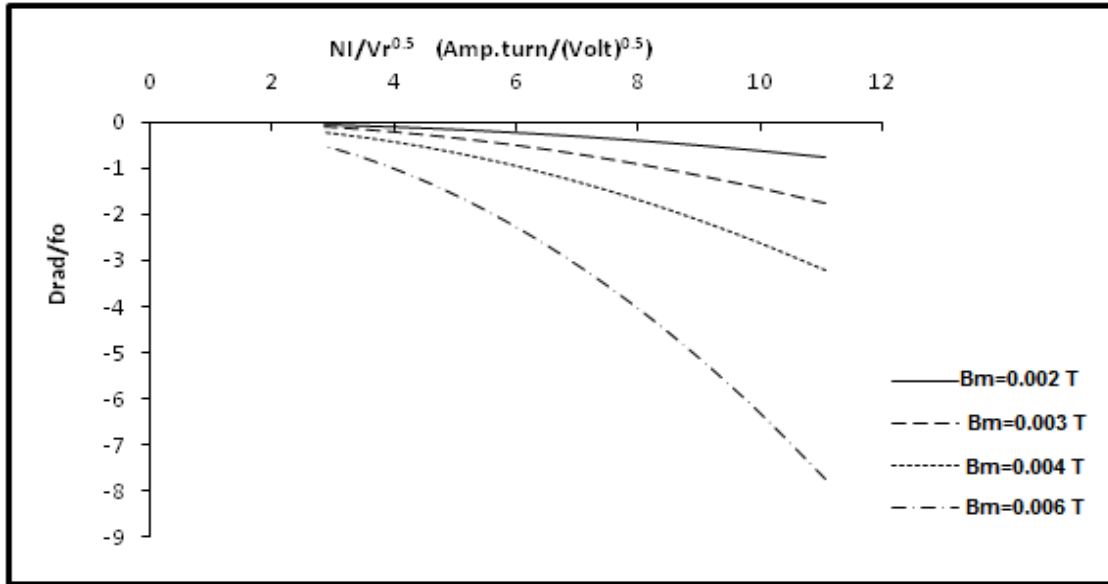

Figure (3-35): Relative radial aberration coefficients as a function of the excitation parameter $\left(\dfrac{NI}{\sqrt{V_r}}\right)$ for different values of the maximum magnetic flux density.

From this figure one can find that the values of the relative radial aberration coefficients D_{rad}/fo decrease as the excitation parameter $(\dfrac{NI}{\sqrt{V_r}})$ increases. Also, the results show that the values of the relative radial aberration coefficients D_{rad}/fo decrease when the maximum magnetic flux density (B_m) increase and the best values are found at the maximum magnetic flux density equal to 0.006 Tesla.

Table 5: The minimum aberration coefficients for different values of the Maximum magnetic flux density (B_m =0.002, 0.003, 0.004 and 0.006 Tesla).

Aberration coefficients	Maximum magnetic flux density (B_m)
C_s = -0.317	0.002 Tesla

$C_c = 0.034$	0.002 Tesla
$D_{sp} = 1.58 \times 10^{-6}$	0.002 Tesla
$D_{rad} = -7.747$	0.006 Tesla

Chapter Two

Theoretical Considerations

2-1 Introduction

A charge particle beam is a group of particles that have about the same kinetic energy and move in about the same direction. The high kinetic energy and directionality of charge particles in beams make them useful for application [32].

Charged particle beams have continually expanding applications in many branches of research and technology recent active areas include flat-screen cathode-ray tubes, and beam lithography for microcircuits, scanning electron microscopy SEM and transmission electron microscopy TEM [32].

2-2 Flux Density Distribution Models of Magnetic Lenses:

The equation of the paraxial ray equations reveals that there is no way for determining electron beam trajectory without knows the axial magnetic field distribution *B(z)*. Different mathematical models are used to explain the axial flux density distribution of the magnetic lenses and in the following the some of these models [9]:

1- Glaser's bell-shaped model:

In this model, the axial distribution of magnetic field B(z) is given by [33]:

$$B(z) = \frac{B_m}{1 + (z/a)^2} \tag{2-1}$$

where B_m is the maximum magnetic flux density, z is the optical axis of system and a is the half-width at half maximum.

2- Related bell-shaped curves:

In particular to the case $n = 3/2$, the field of a single turn, $n = 2$ and $n = \infty$, for which the distribution becomes Gaussian with suitable weighting and given by [33].

$$B(z) = \frac{B_m}{(1 + z^2 / a^2)^n}$$ (2-2)

3- Grivet- lens model:

In this model B(z) is given by :

$$B(z) = B_m \sec h \ (z / a)$$ (2-3)

4- The exponential model:

$$B(z) = B_m \exp(-z / a)$$ (2-4)

2-3 Paraxial - Ray Equation in Magnetic Field

The paraxial ray equation in axially symmetric magnetic fields can be written as [34, 35]:

$$r''(z) + \frac{e}{8m V_r} B^2(z) r - \frac{P_\theta^2}{2m e V_r r^3} = 0$$ (2-5)

where e and m are the charge and mass of electron respectively, P_θ is the initial canonical angular momentum which is given by:

$$P_\theta = \frac{-e B(z_o) r_o^2}{2 m}$$ (2-6)

and r(z) is the radial displacement of the beam from the optical axis z, $r''(z)$ the second derivative of r(z) with respect to z, r_o is the object plane, V_r is the relativistically corrected accelerating voltage which is given by [9]:

$$V_r = V_a (1 + 0.978 \times 10^{-6} V_a)$$ (2-7)

where V_a is the accelerating voltage.

If $P_\theta = 0$, i.e. electron start from the object displaced outside the magnetic field, equation (2-5) becomes linear using the substitution, $u = r_b \exp(i\alpha)$, where α is the additional angle of rotation of meridian plane which is given by [2]:

$$\alpha(z) = \sqrt{\frac{e}{2mV_r}} \int\limits_{z_o}^{z} B(z)\, dz$$ (2-8)

and $\alpha(z_o) = 0$,

one can express the trajectory adjacent to it and get a linear equation:

$$r'' + \frac{e}{8mV_r} B^2(z)\, r = 0$$ (2-9)

It can be easily realized from equation (2-9) that the force driving the electrons towards the axis which is directly proportional to the radial distance r. This is the principle of a focusing field. Futhermore, this force is proportional to the square of the magnetic flux density which means that if the direction of the magnetic field is reversed by reversing the current, the direction of the force towards the axis should not change, i.e. there will be no change in the focus [8].

If u_1 and u_2 are the linearly independent solutions of the linear equation with the initial conditions.

$$u_1(z_o) = 0 \qquad\qquad\qquad u'_1(z_o) = 1$$
$$u_2(z_o) = 1 \qquad\qquad\qquad u'_2(z_o) = 0$$ (2-10)

The paraxial equations which describe electron trajectories in the axial magnetic lens which are given by equation (2-5) and equation (2-9) can be solved by considering the initial conditions for r and $\emptyset$ is given by [2]:

$$r(z_o) = r_o \qquad\qquad\qquad r'(z_o) = \theta_o$$
$$\phi(z_o) = 0 \qquad\qquad\qquad \phi'(z_o) = 0 \qquad\qquad (2\text{-}11)$$

Then the solution of equation (2-5) can be written as:

$$r(z) = |u| = r_o \left[(\frac{\theta_o u_1}{r_o} + u_2)^2 + \sqrt{\frac{e}{8mV_r}} \, B^2(z_o) \, u^2_1 \right]^{1/2} \qquad (2\text{-}12)$$

$$\phi(z) = \sqrt{\frac{e}{8m \, V_r}} \int\limits_{z_o}^{z_i} B(z)\, dz + \arg(u) \qquad (2\text{-}13)$$

And the basic trajectory is described by:

$$r_b(z) = r_o \left[u_2{}^2 + \sqrt{\frac{e}{8m \, V_r}} \, B(z_o)^2 \, u_1{}^2 \right]^{1/2} \qquad (2\text{-}14)$$

Since r_o is the object point and θ_o is the initial angle. Let the trajectory of an electron starting from the specimen go through the magnetic lens described by Glaser's bell-shaped field distribution [33]:

$$B(z) = \frac{B_m}{1 + (z/a)^2} \qquad (2\text{-}15)$$

This lens has field strength with maximum value B_m at the origin of the coordinate system, and a is the half-width at half maximum, w is the full width at half maximum of the field. Then u_1 and u_2 have the following form:

$$u_1 = \frac{-a}{w} \sin\left[w(\phi - \phi_o)\right] \sin(\phi_o) \sin(\phi) \qquad (2\text{-}16)$$

$$u_2 = \frac{\sin(\phi_o)\sin[w(\phi-\phi_o)]}{\sin\phi}\sin[w(\phi-\phi_o)] \qquad (2\text{-}17)$$

$$z = \cot\phi \qquad\qquad z_o = \cot\phi_o \qquad (2\text{-}18)$$

2-4 Aberration of an Axially Symmetric Magnetic Lens

The theory of aberrations is the most extensively studied area in both light optics and electron optics. Intensive investigations of aberrations in axially symmetric magnetic lenses were carried out since in the 1930 in connection with studies of the electron transmission microscope problem. Their implementation provides the creation of an ideal lens that forms stigmatic and similar images, these assumptions:

1- Rigorous axial symmetry.

2- Paraxial trajectory approximation.

3- Energy homogeneity, including the absence of time dependent process.

4- Negligible space-charge fields and small effect of electron diffraction.

Violation of at least one of these conditions leads to aberrations that are responsible for blurred or distorted images and complicate beams transport problems [36].

The importance of a particular aberration depends on the function of the magnetic lens. For an objective lens, only the spherical and chromatic aberrations are important, since the electron-optical limit of resolution is set by the combined effects of electron wavelength and the spherical aberration. For intermediate and projector lenses, the radial and spiral distortions are the most important; they cause a shift of the image point with no blurring. Hence, in the present work computation will be made for these important defects [36].

2-4-1 Spherical aberration

The origin of this defect can be described with aid of diagram shown in figure (2-1), which reveals two different sorts of electrons rays interring a thin lens parallel to the optical axis, but converges to different axial points. From figure (2-1) one may see that electrons traveling close to the optical axis (so-called paraxial rays, $r \approx 0$) are brought to a focus F (a distance f from the centre of the lens) at the Gaussian image plane, whereas electrons which arrive with a non-zero r-coordinate are focused closer to the lens (at point F_1, a distance f_1 from the centre of the lens) resulting the spherical aberration defect [37].
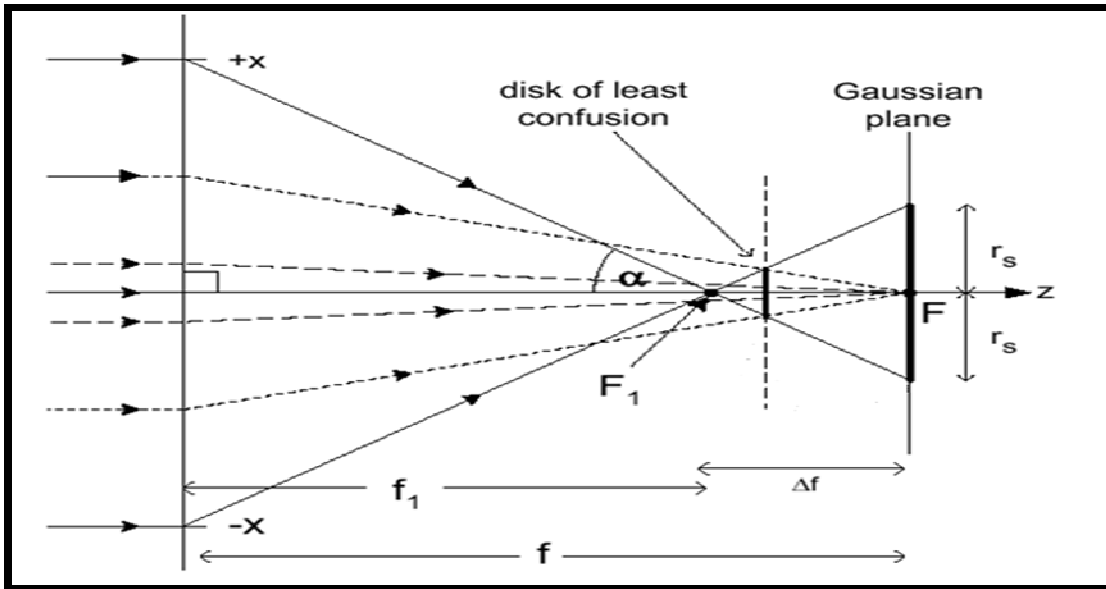
Figure (2-1): The diagram of spherical aberration [37].

When these non paraxial electrons arrive at the Gaussian image plane, they will be displaced radically from the optic axis by an amount r_s given by [37]:

$$r_s = C_s \, \alpha^3 \tag{2-19}$$

where C_s is known as the coefficient of spherical aberration of the lens and α is acceptable half angle. Note that since α (in radian) is dimensionless, C_s must have the dimensions of length.

Thereby, all of the electrons confined within a redial distance *r* are arrived at the Gaussian image plane within a disk of radius r_s usually named by disk of confusion. The spherical aberration defect is the same for all of the points in the image and is the only geometrical aberration that does not disappear on the axis [38].

The spherical aberration coefficient*s* C_s of an axially symmetric magnetic field is given by [36]:

$$C_s = (e/128mV_r) \int_{z_o}^{z} r^4 \left[(3e/mV_r) B^2(z) + 8B'^2(z) - 8B^2(z)(r/r)'^2 \right] dz \quad (2-20)$$

where *r* is the solution of the paraxial ray equation with an initial condition depending of the operation mode. The integration covers the whole interval from object plane z_o to image plane z_i.

2-4-2 Chromatic aberration

In light optics, chromatic aberration arises from the spread of wavelengths of light passing through a lens, coupled with a dependence of refractive index with wavelength which known as dispersion. In electron optics, electron wavelength depends on the momentum or kinetic energy of each particle, so if the electrons have a spread in kinetic energy, one might expect a variation in focusing power of a magnetic lens [1].

Actually, Spread in kinetic energy may be due to:

1- Variation of kinetic energy of the electrons emitted from the electron source. For example, electrons emitted by a heated-filament source have a thermal spread (~kT, where T is the temperature of the emitting surface) due to statistics of the thermionic emission process.

2- Fluctuations in the potential applied to accelerate the electrons. Although high-voltage supplies are stabilized as well as possible, there is always some remaining drift (slow variation) and ripple (ac component) in the voltage.

3- Energy losses due to inelastic scattering in the specimen, in the case of imaging lenses which follow the specimen in a TEM column. This is also a statistical process: not all electrons lose the same amount of energy, resulting in an energy spread. Chromatic aberration would result in additional image blurring which can be characterized in terms of disk confusion, in away similar to that of spherical aberration. Its radius can be estimated with the aid of the lens equation and simple geometric optics. Consider an axial point source of electrons (object distance u) which is imaged to a point (image distance v) for electrons of energy E_0 as is shown in figure (2-2).
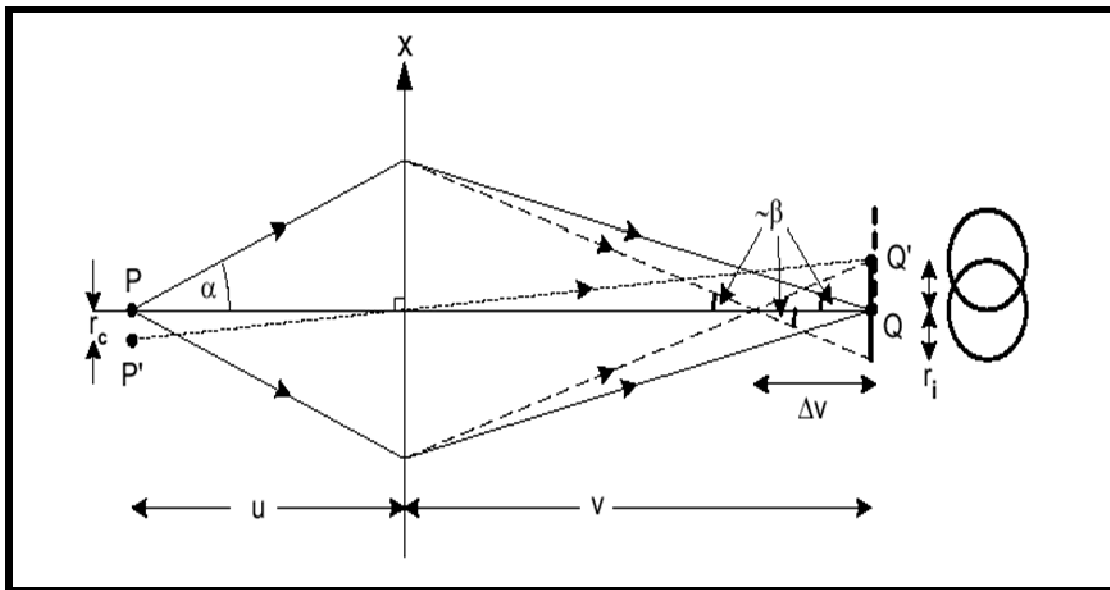

Figure (2-2): The diagram of chromatic aberration [1].

Resulting from chromatic aberration. With two object points, the image disks overlap [37].

Electron of energy E_o- Δ E_o will have in image distance v- Δ v and arrive at the image plane a radial distance r_i from the optic axis. If the angle β of the arriving electrons is small [37].

$$\Delta r_i = \Delta v \tan \beta \approx \beta \Delta v \qquad (2\text{-}21)$$

The loss of spatial resolution due to chromatic aberration is therefore [37].

$$\Delta r_c = \alpha C_c (\Delta E_o / E_o) \qquad (2\text{-}22)$$

The chromatic aberration coefficients C_c of an axially symmetric magnetic optical element is given by [1]:

$$C_c = (e/8mV_r) \int_{z_o}^{z} B^2(z) h^2(z) \, dz \qquad (2\text{-}23)$$

Thus, h(z) is given by [20]:

$$h(z) = f \, r(z) \qquad (2\text{-}24)$$

where f is the focal length. The integration covers the whole interval from object plane z_o to image plane z_i.

2-4-3 Radial distortion

The problem of aberration in the projector lens is different from that in the objective, since the aperture angle of imaging pencil entering the projector lens is very small. However, the spherical and chromatic aberration which have been shown to be proportional to the aperture angle do not in practice affect the reliable resolving power (i.e., the sharpness of the final image) because the magnification required by the projector is only of the order of 300X [39]. While the presence of spherical aberration in the projector lens doesn't cause a significant spread of each image point, another geometrical aberration called radial distortion produces a variation in magnification across the image as a whole. Since the outer parts of the magnetic field of the lens are relatively strong,

pencils of rays which pass this region are refracted more sharply than paraxial pencils. This results in the off-axial pencils crossing the axis earlier and thus striking the image plane at a greater distance from the axis than expected for ideal lens, as shown in figure (2-3a).
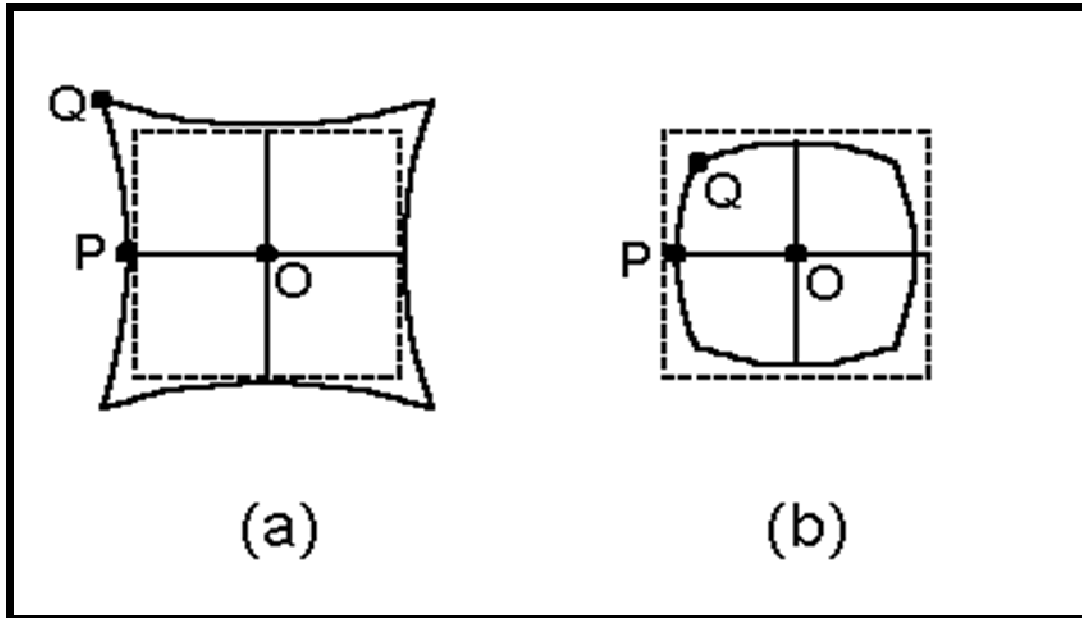
Figure (2-3): (a) Square mesh (dashed lines) imaged with pincushion distortion (solid curves); magnification M is higher at point Q than at point P. (b) Image showing barrel distortion, with M at Q lower than at P[1].

As a result, the peripheral region of the image is more magnified than the paraxial region. When this is the case the resultant distortion is known as pincushion distortion which is observable especially when the power of the projector lens is high [39]. It has been shown that the radial distortion $(\Delta\rho/\rho)_r$ is given by (see figure 2-4) [13]:

$$(\frac{\Delta\rho}{\rho})_r = C_r\,(\frac{r}{R})^2 \qquad\qquad (2\text{-}25)$$

where C_r is the radial distortion constant and R is the bore radius of the projector lens. For the pincushion distortion the value of C_r is positive. When C_r is negative the radial distortion is called barrel distortion. This is illustrated in

figure (2.3b). This sort of radial distortion occurs when the lens is used as a DE magnifying lens [40]. In order to compare different projector lenses, the radial distortion has been expressed in terms of a dimensionless quantity called radial quality factor Q_r [41], as follows:

$$(\frac{\Delta\rho}{\rho})_r = Q_r^2 (\frac{\rho}{b})^2 \qquad\qquad (2\text{-}26)$$
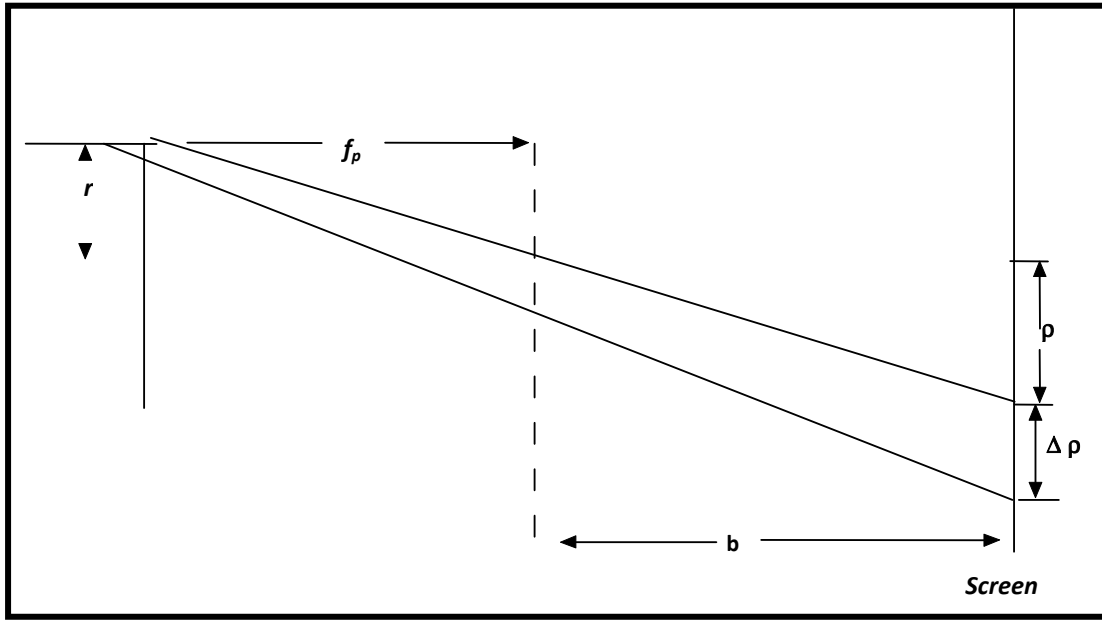
Figure (2-4): The diagram illustrates the effect of radial distortion [40].

The quality factor is given by $Q_r = (D_{rad})^{1/2} f_p$, where $D_{rad} = C_r /R^2$ is the radial distortion coefficient and f_p is the projector focal length.

In the present work the radial distortion coefficient D_{rad} has been calculated using the following integral equation [8]:

$$D_{rad} = (e / 128 \, m V_r)$$

$$\int_{z_o}^{z} [\,(3\,e\,B^4(z)/mV_r + 8\,B'^2(z))\,r_\alpha\,r_y{}^3 - 4\,B^2(z)\,(r_y'^2\,r_\alpha\,r_y + r_y'\,r_y{}^2\,r'\alpha)]\,dz$$

$$(2\text{-}27)$$

where r_α and r_γ are the two linearly independent solutions of the paraxial-ray equation (2-10). The limits of integration are the two terminals points z_o and z_i of the magnetic field.

2-4-4 Spiral distortion

This sort of geometrical aberration has more than one name, such as anisotropic distortion and rotational distortion. It occurs in magnetic lenses only as shown in figure (2-5).
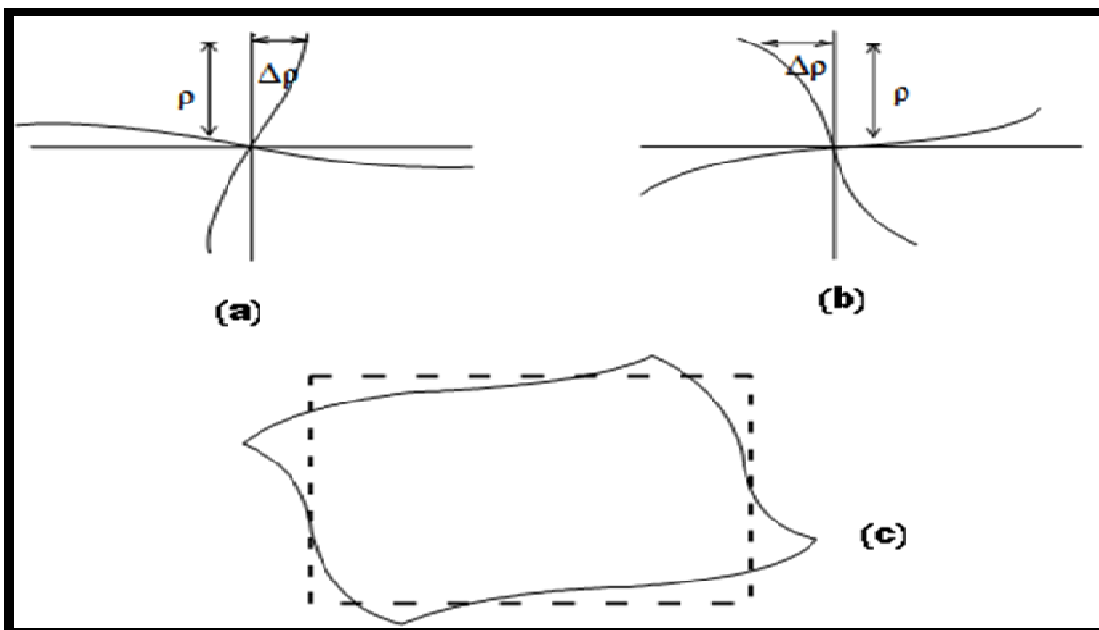
Figure (2-5): The diagram of spiral distortion [13].

The broken lines represent the Gaussian image while the spiral solid lines show the distorted image from which the name is derived. When the lens current is reversed the direction of the field *B(z)* is reversed and the sense of rotation of the electron is also reversed. As a consequence, the image had shown in figure (2-5a) changes to that of figure (2-5b).

It has been shown that the spiral distortion $(\Delta\rho / \rho)_{sp}$ is given by [13]:

$$(\frac{\Delta\rho}{\rho})_{sp} = C_{sp} (\frac{r}{R})^2 \qquad\qquad (2\text{-}28)$$

where C_{sp} is the spiral distortion constant. In a manner similar to that of radial distortion, spiral distortion can be expressed in terms of the spiral quality factor Q_s as follows [41]:

$$(\frac{\Delta\rho}{\rho})_{sp} = Q_s^2 \, (\frac{\rho}{b})^2 \tag{2-29}$$

The quality factor is given by $Q_s = (D_{sp})^{1/2} f_p$, where $D_{sp} = C_{sp}/R^2$ is the spiral distortion coefficient which is determined in this work by means of the following formula [16]:

$$D_{sp} = \int_{z_o}^{z} [\frac{1}{16}(e/mV_r)^{1/2} \, r_y'^2 \, B(z) + \frac{3}{128}(e/mV_r)^{3/2} \, r_y^2 \, B(z)] \, dz \tag{2-30}$$

2-5 Aberration Correction

The correction of aberration coefficients of the electron microscope was started at 1936 by Scherzer. Aberration correction is the long story of many seemingly fruitless efforts to improve the resolution of electron microscopes by compensating for the unavoidable resolution-limiting aberrations of round electron lenses over a period of 50 years. The successful breakthrough, in 1997, can be considered as a quantum step in electron microscopy because it provides genuine atomic resolution approaching the size of the radius of the hydrogen atom [42].

From analysis of the basic properties of electric and magnetic field. The German Scientist Otto Scherzer showed that a conventional electron lens must suffer from spherical and chromatic aberration, with aberration coefficients that are always positive, therefore one cannot eliminate lens aberrations by careful shaping of the lens polepieces, where a spherical lens can be fabricated with zero C_s. [1].

With the realization of the Rose corrector the old dream of electron optics to be able to construct spherical aberration-corrected lens systems has come true. Today, a new generation of commercial transmission electron microscopes is on the market making aberration-corrected high-resolution imaging available to a growing group of researchers, in particular and in materials science [43].

Aberration-corrected transmission electron microscopy allows us to image the structure of matter at genuine atomic resolution. A prominent role for the imaging of crystalline samples is played by the negative spherical aberration imaging (NCSI) technique. The especially high contrast observed under these conditions owes its origin to an enhancing combination of amplitude contrast due to electron diffraction channeling and phase contrast [28]. With the extraordinary results presented therein, this study has demonstrated the potential of the new technology. On the other hand, it has also shown that the techniques which have to be applied to obtain optimum results are quite elaborate and are by far not routine. Interesting, also from a science-sociological point of view, is the fact that the general scientific community appears not to be prepared for the new qualities offered by aberration-corrected transmission electron microscopy [44, 45, and 46]. The benefit of the negative-spherical-aberration imaging technique is used to correct the aberration transmission electron microscope to reach a high-resolution transmission electron microscope (HRTEM). Where the spherical aberration C_s was be tuned to negative values, resulting in a novel imaging technique, which is called the negative spherical aberration coefficients C_s imaging (NCSI) technique [29].

Chapter One

Introduction

Electron optics has much in common with light optics. We can imagine individual electrons leaving an object and being focused into an image, analogous to visible-light photons. As a result of this analogy, each electron trajectory is often referred to as a ray path.

At the end of nineteenth century, it was found that an axially symmetric magnetic field has a focusing effect on an electron beam in a cathode ray oscillograph, it acts as a lens. The effect is similar to that of a glass lens on light. This effect was first investigated by Busch in 1926 [1].

The theory of electron movement through magnetic fields attracted scientists' attention before electron optics was established as a discipline, it may be noted that in 1922 the Russian physicist Boguslawski considered non-uniform magnetic fields where the angular rotation momentum is conserved [2].

Electron optics, in fact is based on two fundamental discoveries presented by De Broglie in 1925 and Busch in 1927. De Broglie postulated on ground of theoretical considerations that one must attribute a wave with each moving particle. Two years later, Busch discovered that the magnetic field of solenoid acts upon an electron in a way exactly similar to that of a glass lens on the light rays [3].

That lead Ruska and Knoll to invent the transmission electron microscope (TEM) in 1932, were the first to recognize the importance of the concentration of the field distribution by an iron yoke and applied it to the production of lenses. The concentration of the magnetic field made it possible to produce an electron microscope with magnification higher than

the optical microscope. Their idea of the magnetic lens is still the basis of lenses at present [4, 5].

In 1943, Grunberg developed a general theory of the focusing action of electrostatic and magnetic fields by describing the path of the main trajectory and knowing the potential distribution along the main paths of adjacent trajectories in the field of arbitrary form [6].

In many electron beam instruments, such as scanning electron microscopes and scanning electron beam lithography systems are usually use a magnetic lens to focus electron beam, and magnetic deflection coils mounted within the lens [7].

According to that, electron optics becomes a theory and practice of production, controlling and utilization of charged particle beam. In other word, one may say that the branch of physics that deals with the properties of charged particle beams motion throughout electromagnetic field is known as electron optics [8].

With the analogy between light and electron optics there are fundamental limitations that should be taken into account. Some of these limitations are listed as follows **[8]**:

1- In light optics, refractive index of light lenses changes abruptly between materials of different indices of refraction. In electron optics, the changes are continuous.

 2- Both the energy and momentum of the electron are continuously variable and can be changed arbitrarily. This is not the case in light optics.

3- A good vacuum must be satisfied for traveling of charged particle beams due to the rapid absorption and scattering of particles by gases, while light rays are free.

4- Almost all lenses in electron optics are convergent, while in light optics

convergent as well as divergent lenses can be used.

1-2 Electron Lenses

Electron lens can be defined as an instrument which collects a moving beam of charged particles or focuses them to the same point. Therefore, the action of electron lenses on an electron (or any charged particle) beam is a close analog to that of convex glass lenses or eye on ray of visible light passing through it. The essential difference between the electron lens and the glass lens is that the electron lenses are concerned with continuously varying index of refraction that always changes abruptly **[9]**.

Electron lenses can be categorized into three main types namely, Electrostatic Lenses, Permanent Magnetic Lenses and Magnetic Lenses **[9]**.

1-2-1 Magnetic lenses

Magnetic lens can be defined as an axially rotational symmetrical magnetic field that acts upon a charged particle beam passing through it, in a way similar to that of a converging lens when it deals with light passing through it. Hence, any rotationally symmetric magnetic field has imaging properties. The simplest magnetic lens is an axially symmetric iron-free coil. Whereas in the modified lenses this coil will be counterpane by iron circuit [10].

There are two effects of a magnetic electron lens on the moving electron beams, the first one, is a deflection towards the optical axis identically to the focusing effect of a converging lens in light optics. The second is an additional rotation around the optical axis [11].

1-2-2 Types of magnetic lenses

Magnetic lenses can be classified from many various points of view, for example:

1- One can talk about bounded lenses whether the boundaries of the lens can or cannot found.

2- Strong or weak lenses depending on whether their focal points are situated inside or outside the field.

3- Thick or thin lenses.

4- Symmetrical or asymmetrical lenses depending upon whether their exist middle plane perpendicular to the optical axis about which the geometrical arrangement of the lens is symmetrical or not [10 and 9].

5- Magnetic electron lenses can be classified according to the number of their polepiece in to three types: single polepiece lens, double pole piece lens and triple polepiece lens, also iron-free lenses are one of magnetic lenses types. So these types will be explained as the following [9]:

a- Single pole piece magnetic lens

In 1972 Mulvey introduced a new design of magnetic lens named 'Snorkel' lens. When the double polepiece magnetic lens is divided into two halves from the middle a single polepiece magnetic lens can be obtained by removing one half. The single polepiece magnetic lens has been taken a great interest in the electron optical instruments. The absence of the bore in the single polepiece lens makes fabrication of the lens easier. The single polepiece lens has the advantage that the entire lens can be physically situated outside the vacuum chamber as shown in figure (1-1). The axial magnetic flux density distribution of the single polepiece lens can be pushed away from the lens profile itself making the optical properties of the lens less

dependent on the imperfections in the iron circuit and the energizing coil [12, 4].
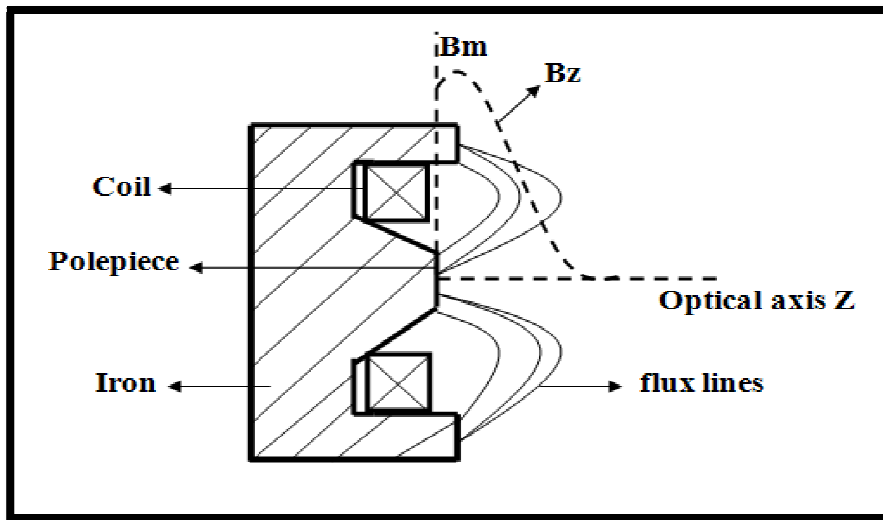

Figure (1-1): Cross-section of single polepiece magnetic lens [4]

b- Double pole piece magnetic lens

   This type of magnetic lenses consists of insulated wire or tape windings made of conducting material (usually copper) surrounded by a ferromagnetic material core of high magnetic permeability which was designed by Ruska in 1933. The core has coaxial circular bore of diameter *"d"* along the optical axis to allow the electrons beam to pass through an air gap of width *"S"* formed in the iron circuit between the two polepieces as shown in figure (1-2). The properties of these lenses are expressed in terms of the ratio (S/d) [13].
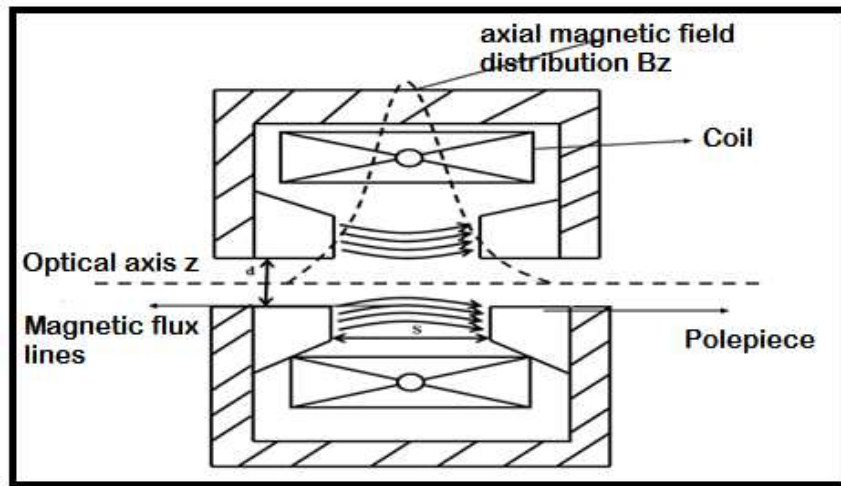
Figure (1-2): Cross-section of double polepiece magnetic lens [13]

Symmetrical double polepiece magnetic lens could be achieved when the axial bores between the two polepieces are identical, while asymmetrical lens be held when the axial bores are not identical.

c- Triple pole piece magnetic lens

Doublet lens consists of two magnetic electron lenses of two air gaps and it is also called triple polepiece magnetic lens [14]. The two magnetic lenses of the triple lens may be symmetrical or asymmetrical depending on the design of each lens as in figure (1-3).
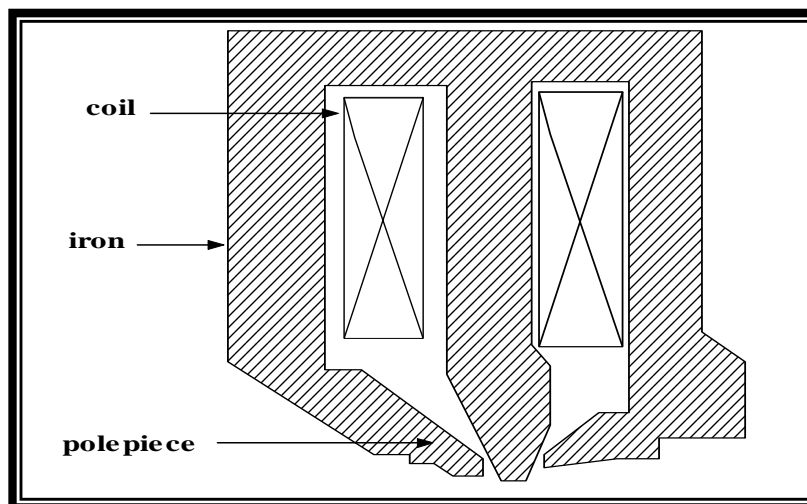

Figure (1-3): Cross-section of triple polepiece magnetic lens [14].

d- Iron-free lens

This lens is the simplest probe-forming device; it consists of coils made from metallic conductor wire or tape windings wound on non-magnetic core as in figure (1-4).
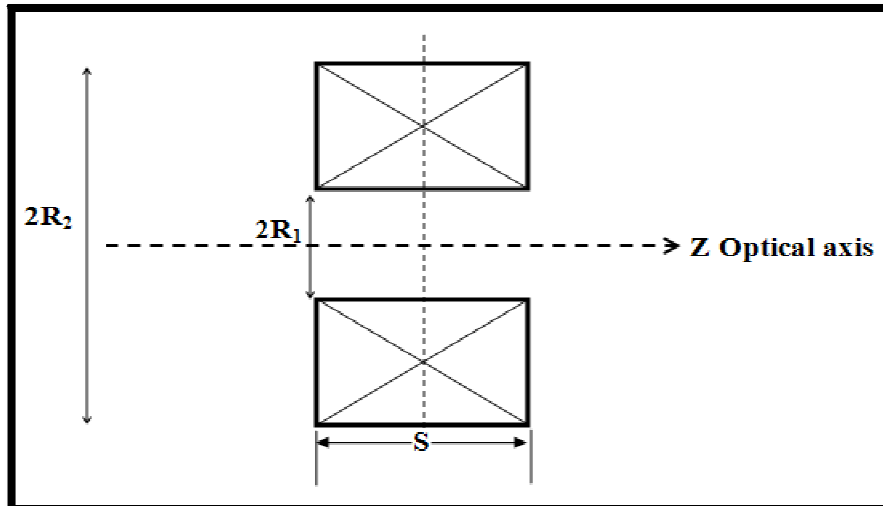

Figure (1-4): Cross-sections of Iron-free rectangular [15].

One advantage of the iron-free coils is their size reduction with respect to the iron circuit lenses. It is therefore desirable to describe some recent investigations of iron-free objective lenses that offer the possibility of developing electron optical instruments, both with and without the use of superconducting windings [15].

1-3 Advantages of a Magnetic Lens

Magnetic lenses are generally preferred for electron microscopy, because it has higher accelerating voltages this permit better image resolution. Magnetic lenses also provide the lower aberrations, for the same focal length by comparison with electrostatic lens, further improving the image resolution, lens aberrations are also reduced by making the focal length of the objective lens small, implying a magnetic immersion lens with the specimen present within the lens field [1].

1-4 Comparison between Numerical and Analytical Method

A part from the measurement procedure, lens properties may be determined by means of two entirely different approaches namely, analytical and numerical approach. The numerical approach is used to be a powerful technique for determination of the electron lens properties. However, in practice numerical approach still considered to be the best, but its results are less accurate than the analytical approach, because it provides a large degree of freedom to handling the considered problem. The analytical solutions have very definite advantages over numerical approach. There are numerous reasons for this [9]:

1- Numerical solutions always give a more or less accurate approximation

   while analytical is exact.

2- Analytical solutions provide insight and allow classification according to

   the influence of different parameters on the solution.

3- They can be verified by inversion.

4- They extend the frontiers of tractability.

5- They provide simple means for comparing different numerical techniques.

   The disadvantages of the analytical approach can be given by the following [9]:

1- The axial field distribution of practical electrode and polepiece configurations can very seldom be expressed in analytical functions.

2- Even if we know the exact form of rays, it is unlikely that we will be able

   to deduce analytical expressions for the aberration coefficients. The analytical approach was the taken choice.

1-5 Literatures Survey

Theoretical and experimental studies of the magnetic lens have been attempted by many researchers as:

Tsuno and Harada in 1981 studied the minimization of radial and spiral distortion in electron microscopy through the using of a triple polepiece lens [16].

Mulvey studied the use of a single pole electromagnetic lens and showed that it had good electron optical properties [10].

Preikzas and Rose in 1995 introduced a procedure called time dependent perturbation formalism which enables the aberrations of any arbitrary electron optical systems to be calculated [17].

In 1996 Crewe and Kielpinski found that the focal length, spherical and chromatic aberration coefficients of dipoles magnetic lenses could be expressed simply by normalized the dipole moment [18].

Subsequently, Crewe extended the study of two multipole magnetic lenses through numerical and digital methods and obtained some interesting result on the electron optical properties of monopole, dipole and quadrapole lenses [19].

Hawkes in 2002 used the properties of Bessel function to predict the most of the results which were found by Crewe for the same magnetic lenses, where the analytical method was included to obtain the optical properties which were found by Crewe [20].

In 2003 the optical properties of monopole, dipole and quadrupole magnetic lenses had been demonstrated by Liu. The differential algebraic (DA) method and analytical expression were adopted in this study [21].

Cheng et al. had applied the differential algebra method to analyze and calculate arbitrary order curvilinear-axis combined geometric-chromatic aberrations of electron optical systems [22]. Also, the spiral distortion of projector magnetic lenses had been studied by Alamir [23].

In 2004 Crewe studied the focusing properties of magnetic fields of the form $B(z) \, \alpha \, z^n$ for all integer n except the cases when $n = -1$ and $n = 0$. The calculations in this study were achieved by using numerical ray tracing which were carried out for first and second indexes of the zero only [24].

In 2004 Chun-Lin et al. studied the high resolution transmission electron microscopy using a negative spherical aberration. The novel imaging mode for high-resolution transmission electron microscopy was described. The novel imaging mode was based on the adjustment of a negative value of the spherical aberration of the objective lens of a transmission electron microscopy equipped with a multi pole aberration corrector system [25].

In 2005 the spherical and chromatic aberration coefficients for the objective and projector magnetic lenses with the field distribution in the forms of inverse power law were calculated by Alamir to express the magnitude analytically. The results of this study were presented in a Tretenr's form to determine the optimum performance of magnetic lenses [26].

The novel aberration correction concepts were shown by Berend and Harald in 2008. An alternate concept for improving spatial resolution for some experiments in TEM mode was studied with the aid of the spherical aberration correction and monochromatization; in this case the loss in resolution caused by a wide-gap objective lens was compensated by a smaller energy width of the electron beam [27].

Also, an analytical expression for the paraxial trajectory of magnetic lenses was derived by using the analytical approach. And the comparison was made with the results of the numerical approach [2].

One year later, aberration-corrected of transmission electron microscopy was made to allow imaging the structure of matter at genuine atomic resolution. A prominent role for the imaging of crystalline samples was achieved by using the negative spherical aberration imaging (NCSI) technique [28].

The benefit of the negative spherical aberration imaging technique for quantitative HRTEM (High resolution transmission electron microscopy) had been studied by Jia, et al. in 2010. They found that the image contrast which is obtained with the (NCSI) technique was compared quantitavialy with the image contrast formed with the traditional positive C_s imaging (PCSI) technique [29].

In 2012 Clemens and Peter studied the temporal distortion in magnetic lenses. They studied the temporal aberration of femtosecond electron pulses in magnetic lens system [30].

The theoretical and experimental investigation was made to correct the spherical and chromatic aberration by Funio et al. at 2013. The asymmetric spherical aberration correctors were designed for use in the prop and image forming systems at 300 kV to diminish undesired parasitic aberrations. Also the chromatic aberration corrector was investigated using a 30 kV transmission electron microscope [31].

1-6 Aim of work

The aim of present work is to study and determination the optimum optical properties of magnetic lens using analytical method. This aim can be achieved via reduction the values of aberration coefficients or reach to negative values of these aberration coefficients, which can be used as corrector in the optical systems.

The analytical expression is used to find the paraxial trajectory of electron beam in a magnetic lens and this trajectory will be used to study the optical properties of magnetic lens; the axial flux density distribution is represented by Glaser's bell-shaped model which gives rise to the minimum spherical, chromatic, spiral and radial distortion aberration coefficients.

Chapter Four

Conclusions and Recommendations for Future Works

4-1 Conclusions

From the results one can conclude that:-

1- The analytical method can be used to give good description to the electron beam trajectory, and this trajectory can be used to find the best optical properties of the magnetic lens.

2- The optimization role can be achieved via changing some effective parameters as the half width at half maximum (a), the maximum magnetic flux density (B_m) and the electron emission angle (θ). Also, the calculations appear that the values of the aberration coefficients are very sensitive to the changing of the effective parameter.

3- One can reach to the negative values of the spherical and spiral distortion aberration coefficients by using the solution electron beam trajectory which due to the analytical solution of the paraxial ray equation, and these negative values can be used as a corrector in the optical system.

4- One can notice that for:

   a- The case of zero initial angular momentum

1- The results of calculations show that the relative spherical, chromatic and spiral aberration coefficients decrease as the half-width at half maximum increase and the lowest results are found at the half-width at half maximum equal to 2.04 mm.

2- The best values of the relative spherical and radial aberration coefficients are occurred at the maximum magnetic flux density equal to 0.004 Tesla.

One can notice that the relative chromatic and spiral aberration coefficients increase when the maximum magnetic flux density (B_m) increase, and the optimum results occurred at the maximum magnetic flux density equal to 0.001 Tesla.

b- The case of non-zero initial angular momentum

1- From the results one can notice that the relative spherical and radial aberration coefficients decrease as the electron emission angle is increasing and the chromatic and spiral aberration coefficients increase as the electron emission angle increase and the best results are found at the electron emission angle equal to 0.2 rad.

2- The lowest results of the relative spherical, chromatic and spiral distortion aberration coefficients can be obtained at the half width at half maximum equal to 2.04 mm, One can notice that the relative spherical, chromatic and spiral distortion aberration coefficients decrease when the half-width at half maximum increase, and the best values of the radial aberration coefficients can be obtained at the half-width at half maximum equal to 2.01 mm.

3- The results of calculations indicate that the relative spherical, chromatic and spiral aberrations coefficients increase at the maximum magnetic flux density (B_m) increase and the best values at maximum magnetic flux density equal to 0.002 Tesla. But the lowest values of the radial distortion aberration coefficients at the maximum magnetic flux density equal to 0.006 Tesla.

4-2 Recommendations for Future Works

The following topics are put forward as future investigations:

1- One can suggest different methods such as differential algebraic method (DA) method to study the optical properties of the magnetic lenses in order to compare this procedure with the calculated results.

2- One can use the analytical method to find the solution of the paraxial ray equation for different models as the Grivet-Lens model, to reach to the optimum optical properties which give the minimum aberration coefficients.

3- The time dependent magnetic field method can be use to find the optimum optical properties for the magnetic lens.

Contents

List of Symbols

Symbol	Definition
a	The half-width at half maximum (mm).
$B_{(z)}$	The axial distribution of Magnetic field of lens (Tesla).
$B_{(m)}$	Maximum magnetic flux density (Tesla).
C_c	Chromatic aberration coefficient (mm).
C_r	Radial distortion constant.
C_s	Spherical aberration coefficient (mm).
C_{sp}	Spiral distortion constant.
D	Diameter of axial bore (mm).
D_{rad}	Radial distortion coefficient (mm).
D_{sp}	Spiral distortion coefficient (mm).
e	The charge of the electron (e =1.6 x 10^{-19} C).
E_o	Energy of electron beam (Joule).
f_p	The projector focal length (mm).
f_o	The objective focal length (mm).
h(z)	The independent solutions of the paraxial-ray equation.
I	Electric current (Amper).

k	Boltzmann constant (k=1.38x10^{-23}J/degree Kelvin).
m	The mass of the electron (m= 9.1 x 10^{-31} kg).
n	Order of multipole or the power of the multipole.
NI	Magnetic lens excitation (Amp.turn).
$(\dfrac{NI}{\sqrt{V_r}})$	Magnetic lens excitation parameter (Amp.turn/(Volt)$^{0.5}$).
P_θ	Initial angular momentum (Kg.m^2.s^{-1}).
Q_r	Radial quality factor.
Q_s	Spiral quality factor.
R_1,R_2	Inner and outer radii of coil respectively (mm).
r(z)	Trajectory radial high along axis outside the magnetic field (mm).
$r_b(z)$	Trajectory radial high along axis inside the magnetic field (mm).
r_o	The object plane.
$r^{"}$	The second derivative of r(z).
r_s	The radius of confusion disk (mm).
r_α ,r_y	Special solutions of paraxial ray equation.
S	Width of air gap of polepiece (mm).
T	Temperature of the emitting surface (Kelvin).
u_1, u_2	The two linearly independent solutions of the linear equation.

V_a	The accelerating voltage (Volt).
V_r	Relativistically corrected accelerating voltage (Volt).
w	The full width at half maximum of the field (mm).
z	The optical axis of system (mm).
z_o	Object plane position (mm).
z_i	Image plane position (mm).
θ	Electron emission angle (rad).
θ_o	Initial electron emission angle (rad).
α	Additional angle of rotation meridian plane (rad).
$\emptyset(z_o)$	Initial conditions at the image plane.
ΔE_o	Fluctuation in the electron beam energy (Joule).
Δr_i	Fluctuation in the electron beam focus at the image side (mm).
ρ	Total charge density.
$(\Delta\rho/\rho)_r$	Radial distortion amount.
$(\Delta\rho/\rho)_{sp}$	Spiral distortion amount.
' , "	First and second derivative with respect to z-axis (d/dz) and (d^2/dz^2), respectively.

List of Abbreviations

Abbreviation	Definition
DA	Differential algebraic.
HRTEM	High resolution transmission electron microscope.
NCSI	Negative spherical aberration imaging technique.
SEM	Scanning electron microscope.
TEM	Transmission electron microscope.

[1] Egerton, R.F. (2005)

Physical Principle of Electron Microscopy.

Springer: ISBN.

[2] Melnikov, A.A. and Potapkin O.D. (2008)

On Electron Movement through Magnetic Electron Lens.

Physics Procedia **1**, 207-215.

[3] Harald, H.R. (2008)
Geometrical Charged-Particle Optics.

Springer-Verlag, Berlin.

[4] Mulvey, T. and Newman ,C.D. (1974)

New Experimental Lens Designs for High Voltage Electron Microscopes.

High voltage electron microscopy, ed.P.R.Swan, C.J.Humbherys and M.J.Goringe, pp.98-102. Academic: London.

[5] Ruska, E. (1980)

The Early Development of Electron Lenses and Electron Microscopy.

Hirzel Verlag, Stuttgart.

[6] Grunberg, G.A. (1948)
 Selected Problems of Mathematical Theory of Electric and Magnetic Phenomena.
 A.N. USSS in Russian.

[7] Lencova B. (2001)

Recent Development in Methods for Electron Optical Computation Microscopy.

 Barcelona **93**, 432-439.

[8] El-Kareh, A. B. and El-Kareh, J. C. J. (1970)

Electron Beams Lenses and Optics.

Vol. **1** and **2**, Academic Press: New York and London.

[9] Szilagyi, M., (1988)

Electron and Ion Optics.

Plenum Press: New York and London.

[10] Hawkes, P. W. (1982)

Magnetic Electron Lenses.

Springer-Verlag, Berlin.

[11] Labar, J. L. (2002)

Introduction to Electron and Microscope: Electron Optics, Interactions and Signals.

EMAS-2002, Szsyrk (Poland).

[12] Mulvey ,T. and Newman, C.D. (1973)
New Electron Optical System for SEM and STEM.
Scanning Electron Microscopy: system and applications 1973, ed. W.C.Nixon,
Inst.phys.Conf.Ser, No.**18**, 16-21.

[13] Libmann, G. and Grad, E. M. (1952)

Image Properties of a Series of Magnetic Electron Lenses.

Proc. Phys. Soc. London, **B1** 1951-1956.

[14] Tsuno, K. and Harada, Y. (1981)

Elimination of Spiral Distortion in Electron Microscope Using an A Symmetrical Triple Polepiece Lens.

J. Phys. E: Sci. Instrum. **14** 955-960.

[15] Alamir, A.S.A. (2000)

High Voltage and High Current Density Objective Lens.

Chinese J.Phys.**38**, No.2-1, 139-145.

[16] Tsuno, K. and Harada, Y. (1981a)

Minimization of Radial and Spiral Distortion in Electron Microscopy Through the Use of a Triple-PolePiece Lens.

J. Phys. E: Sci. Inst., **14**, 313-319.

[17] Preikszas D. and Rose H., (1995)
Procedures for Minimizing the Aberrations of Electromagnetic Compound Lenses
Optik, **100**, 4, pp. 179-187.

[18] Crewe, A.V. and Kielpinski, D. (1996)
Electron Focusing Using Dipole Lenses.

Optik **103,** 167-170.

[19] Crewe, A.V. (2001)

On the Peculiarities of Monopole and Multipole Focusing.

Optik **112**, No. 4, 181-183.

[20] Hawkes, P.W. (2002)
On the Optical Properties of Magnetic Lenses with Fields of the Form B(z)α z^{-n} n=2,3,4 .
Optik **113**, No. 6, 273-275.

[21] Liu,Z.X. (2003)

Differential Algebra Analysis of Optical Properties of Monopole, Dipole, and Quadrapole Lenses.

Optik **114**, No. 11, 518-520.

[22] Cheng, Tang, Lu and Yao. (2003)

Differential Algebraic Method for Arbitrary Order Curvilinear- Axis Combined Geometric- Chromatic Aberration Analysis.

Division of Communication Engineering, Nanyang Technology University, J. Phys. D: Appl. Phys. **36,** 924-928.

[23] Alamir, A.S.A. (2003b)

Spiral Distortion of Magnetic Lenses with Fields of the Form B(z)α z^{-n}, n=2,3,and 4.

Optik **114**, No. 12, 525-528.

[24] Crewe, A.V. (2004)

Electron Focusing in Magnetic Fields of the Form z^{n}.

Optik **115**, No. 1, 31-35.

[25] Jia, C.L. Lentzen, M. and Urban, K. (2004)

High-Resolution Transmission Electron Microscopy Using Negative Spherical Aberration Microscopy.

Microanal **10,** 174–184.

[26] Alamir , A.S.A. (2005)

On the Optical Properties of Monopole, Multipole, Magnetic Lenses.

Optik **116,** 429-432.

[27] Kabius, B. and Rose, H. (2008)

Advances in Imaging and Electron Physics.

 Vol **153**.

[28] Knut,W. Urban, Jia, C.L. Houben, L. Lentzen, M. Mi, Sh. and Tillmann, K. (2009)

Negative Spherical Aberration Ultrahigh-Resolution Imaging in Corrected Transmission Electron Microscopy.

Phil. Trans. R. Soc, **367,** 3735–3753**.**

[29] Jia, C.L. Houben, L.Thust, A. and Barthel, J. (2010)

On the Benefit of the Negative –Spherical –Aberration Imaging Teqhnique for Quantitative HRTEM.

Ultramicroscopy **110,** 500-505.

[30] Weninger, C. and Baum, P. (2012)

Temporal Distortion in Magnetic Lenses.

Ultramicroscopy **113,** 145-151.

[31] Fumio Hosokawa, Hidetaka Sawada, Yukinito Konodo, Kunio Takayangi and Kazutomo Suenagaz. (2013)

Development of Cs and Cc Correctors for Transmission Electron Microscopy.

Microscopy, doi: 10.

[32] Humphries, S.Jr. (2002)

Charged Particle Beams.

Wiley: New York.

[33] Hawkes, P.W. and Kasper, E. (1989)

Principle of Electron Optics.

Vol.**1** and **2**, Academic press: London.

[34] Martin Reiser. (2008)

Theory and Design of Charged Particle Beams.

 Second update and second edition, Wiley -VCH.

[35] Tzukkerman, I.I., Gosenergoizdat M. (1958)

 Electron Optics in Television.

Pergamon press:New York.

[36] Tsimring, S.E. (2007)

Electron Beams and Microwave Vacuum Electronic.

 Wiley: Canada.

[37] Egerton, R.f. (2007)

 Physical Principles of Electron Microscopy an Introduction to TEM, SEM and AEM.

Wiely : Canada

[38] Hall, P. C. E. (1966)

Introduction to Electron Microscopy.

2nd Ed., Mc Graw-Hill.

[39] Wischnitzer, S. (1981)

Introduction to Electron Microscopy.

 3rd ed., Pergamon Press.

[40] Glauert, A. M. (1974)
Practical Methods in Electron Microscopy.

 North Holland.

[41] Marai, F. Z., and Mulvey, T. (1977)

Scherzer's Formula and the Correction of Spiral Distortion in the Electron Microscope.

Ultramicroscopic **2**, 178-192.

[42] Rose, H. (2009)

Historical Aspects of Aberration Correction Electron Microscopy.

 Vol **58**, 77-85.

[43] Urban, K. W. (2008)
 Studying Atomic Structures by Aberration-Corrected Transmission Electron Microscopy.
Science **321**, 506–510.

[44] Rose, H. (1990)
Outline of a Spherically Corrected Semiaplanatic Medium-Voltage Transmission Electron Microscope.
Optik **85**, 19–24.

[45] Haider, M., Uhlemann, S., Schwan, E., Rose, H., Kabius, B. and Urban, K. (1998)
Electron Microscopy Image Enhanced.
 Nature **392**, 768–769.

 [46] Uhlemann, S. and Haider, M. (1998)
Residual Wave Aberrations in the First Spherical Aberration Corrected Transmission Electron Microscope.
Ultramicroscopy **72**, 109–119.

Republic of Iraq
Ministry of Higher Education
and Scientific Research
Al-Nahrain University
College of Science
Department of Physics

Magnetic Lens Aberration Coefficients Estimation by Using the Analytical Solution for the Paraxial Ray Equation

A Thesis
Submitted to the College of Science/ Al-Nahrain University as a Partial Fulfillment of the Requirements for the Degree of Master of Science in Physics

By
Rasha Yousif Hamad
(B.Sc.in Physics-2011)

Supervised by

Dr.Oday A.Hussein　　　　　　　**Dr.Khalid A.Yahya**
(Assist. Professor)　　　　　　　　　(Assist. Professor)

November　　　　　　　　　　　　　　　Muharram
2013 A.D.　　　　　　　　　　　　　　　1435A.H

جمهورية العراق
وزارة التعليم العالي والبحث العلمي
جامعة النهرين
كلية العلوم
قسم الفيزياء

تخمين معاملات زيوغ ألعدسه المغناطيسية باستخدام الحل التحليلي لمعاده المسار القريب من المحور

رسالة

مقدمه إلى كلية العلوم/ جامعة النهرين
كجزء من متطلبات نيل درجة الماجستير في علوم الفيزياء

من قبل

رشا يوسف حمد

(بكالوريوس - ٢٠١١)

إشراف

ا.م.د.عدي علي حسين   **ا.م.د.خالد عباس يحيى**

محرم   تشرين الثاني

١٤٣٥ هـ   ٢٠١٣ م

بسم الله الرحمن الرحيم

اقْرَأْ بِاسْمِ رَبِّكَ الَّذِي خَلَقَ (١)
خَلَقَ الْإِنْسَانَ مِنْ عَلَقٍ (٢) اقْرَأْ
وَرَبُّكَ الْأَكْرَمُ (٣) الَّذِي عَلَّمَ بِالْقَلَمِ
(٤) عَلَّمَ الْإِنْسَانَ مَا لَمْ يَعْلَمْ (٥)

سورة العلق

الخلاصة

أجريت دراسة نظريه باستخدام ألصيغه التحليلية لمعادله المسار شبه المحوري للإلكترون وذلك لتحديد أفضل الخواص ألبصريه للعدسة المغناطيسية.

تم دراسهة معاملات الزيوغ كمعاملات الزيوغ الكروية، أللونيه، التشويه القطري و اللولبي. اعتمد في هذا البحث أنموذج الشكل ألناقوسي لكلاسر لتمثيل توزيع المجال المحوري للعدسة المغناطيسية. وقد اخذ بنظر الاعتبار حالتين للزخم الابتدائي في الحسابات بوجوده أو عدم وجوده في الحالتين.

إن الوصول إلى امثل النتائج قد أنجز من خلال تغير بعض المعاملات المؤثرة مثل نصف العرض عند نصف الحد الأقصى(a= 2.01, 2.02, 2.03 and 2.04 mm)، والحد الأعلى لكثافة الفيض المغناطيسي (Bm= 0.001, 0.002, 0.003 and 0.004 Tesla) وزاوية انبعاث الإلكترون (θ =0.2, 0.4, 0.5 and 0.6 rad).

من خلال النتائج تبين إن أفضل قيم a تساوي 2.04 mm في حاله وجود أو عدم وجود الزخم الابتدائي في الحسابات. وقد وجد أيضا إن كل من قيم الزيغ الكروي، أللوني والتشويه اللولبي يقل بزيادة a، بينما اقل قيم للزيغ الكروي و التشويه القطري في ألحاله الأولى عند B_m يساوي 0.004 Tesla.

ووجد أيضا أن أفضل الزوايا للإلكترون (θ = 0.2 rad) وهي تتناسب طرديا مع معاملات الزيغ أللوني والتشويه اللولبي.

ومن جهة أخرى تبين إن الزيغ الكروي والتشويه القطري له قيم سالبه وهذه المعاملات ممكن استخدامها كمصحح في المنظومات البصرية.